ABSTRACT

KAKALEY, DANIEL EDWIN. Real-Time Monitoring of Shaft Torque, Axial Translation and Whirl: Applications to High-Speed Aerospace Drivetrains. (Under the direction of Dr. Gregory Buckner).

Since the advent of high-speed rotating machinery, methods have been proposed to accurately monitor drivetrain health, usually based on the measurement or estimation of shaft parameters such as speed, torque, radial deflection and axial translation. Real-time knowledge of these parameters is not only critical to enhancing the safe operation of aerospace drivetrains, it enables the implementation of advanced feedback control systems.

This dissertation focuses on the development and experimental demonstration of a unique non-contacting Variable Reluctance (VR) sensor system that enables simultaneous estimation of shaft speed, torque, axial translation and whirl in high-speed rotating shafts. A novel tooth geometry is introduced which features alternating slants on every third tooth of an otherwise standard toothed wheel. A novel torque and axial processing (TAP) algorithm allows axial translation to be extracted from the VR sensor measurements. Simulations confirm that shaft speed, torque, and axial translation can be accurately estimated based on timing measurements. Experiments conducted on a high-speed driveshaft further validate the TAP approach and reveal that the accuracy of shaft torque estimation improves significantly with axial translation compensation.

A similar algorithm for the VR sensor system enables estimation of shaft synchronous radial whirl in high-speed rotating shafts. This novel shaft whirl estimation (SWE) algorithm allows radial whirl to be extracted from the VR sensor measurements, and is capable of permanent installation in aerospace drivetrains. Simulations confirm that, in addition to shaft

speed, torque and axial displacement, shaft whirl can be accurately estimated based on timing measurements. Experiments conducted on a high-speed driveshaft validate the SWE approach in both steady-state and transient shaft loading conditions.

With this enhanced VR sensor system and signal processing algorithms, significant improvements can be made to existing drivetrain health monitoring and control systems for aircraft. Drivetrain health monitoring is typically integrated during initial aircraft flight tests using off-the-shelf technologies, however, a VR sensor system allows permanent measurement on an aircraft despite the harsh aerospace environment. Due to its permanent, unique measurement capabilities, this dissertation's VR sensing methods and algorithms are currently supporting aircraft control systems during both initial flight testing and production.

Real-Time Monitoring of Shaft Torque, Axial Translation and Whirl: Applications to High-Speed Aerospace Drivetrains

by
Daniel Edwin Kakaley

A dissertation submitted to the Graduate Faculty of
North Carolina State University
in partial fulfillment of the
requirements for the degree of
Doctor of Philosophy

Mechanical Engineering

Raleigh, North Carolina
2019

APPROVED BY:

_____	_____
Dr. Gregory D. Buckner Committee Chair	Dr. Larry M. Silverberg
_____	_____
Dr. Andre P. Mazzoleni	Dr. John E. Thomas

DEDICATION

This study is dedicated to the three people who provided the inspiration for my scientific career: my great grandfather Dr. Claud E. Cleeton (physicist), my grandfather Ed Kakaley (mechanical engineer), and my father Russell Kakaley (mechanical engineer). My education today is a direct result of their support, inspiration, and encouragement.

BIOGRAPHY

Daniel Edwin Kakaley was born in Springfield, Massachusetts to Russell and Rebecca Kakaley. Shortly thereafter, his family relocated to Charlotte, North Carolina for the remainder of his childhood. After high school, he began working at Midrex Technologies in a machine shop and learned the importance of a college education. In 2010 he began his studies at North Carolina State University. During this time, he worked at NASA Glenn as an Aeronautics Academy Intern and Midrex Technologies analyzing the reduction of iron, under the supervision of Greg Hughes, who provided a tremendous example of hard work and inspiration. In the spring of 2013, he graduated with a B.S. in Mechanical Engineering and subsequently began working in Mechanical Research at Lord Corporation under the supervision of Dr. Mark Jolly and Russell Altieri. Concurrent with his work, he graduated with a B.S. in Physics in 2014 and M.S. in Mechanical Engineering in 2015. His work responsibilities focus on developing highly engineered vibration solutions and high-speed powertrain monitoring technologies.

In a partnership between Lord Corporation and North Carolina State University, he conducted his Graduate research under Dr. Gregory Buckner's guidance.

Shortly after beginning work at Lord Corporation, he met his wife, Elizabeth Medlock. With her continual support and encouragement, he has continued his work at Lord Corporation and academic career at North Carolina State University.

ACKNOWLEDGMENTS

I would like to thank Dr. Gregory Buckner and Dr. Mark Jolly for offering their guidance and support on this research and in mentoring me as an engineer. In addition, I would like to thank Lord Corporation for the use of test equipment and financial support, and North Carolina State University for giving me the opportunity to continue my graduate studies. I also wish to thank my committee members, Dr. Larry Silverberg, Dr. Andre Mazzoleni, and Dr. John Thomas, for their time and interest. Finally, I would like to thank my parents, Russell and Rebecca Kakaley, for giving me the opportunity for an education.

TABLE OF CONTENTS

LIST OF TABLES

LIST OF FIGURES

Chapter 1: Introduction

Aerospace industry trends are pushing for increased aircraft power through lighter and more flexible drivetrain components, necessitating the need for real-time torque and drivetrain monitoring technologies to ensure safe operation. Viable monitoring systems must function in harsh environments and provide accurate torque measurements in the presence of axial and radial drivetrain motions. Torque monitoring systems are currently used in various mechanical applications to detect and avoid potentially destructive effects such as torsional resonance [1] or excessive loading [2], and to provide records of machine operating conditions [3] during start-ups, misfires, torque reversals, etc. [4]. Torque measurement allows for immediate corrective action in applications with integrated feedback control algorithms [4-5], including aircraft flight control systems [6].

1.1. Direct Torque Measurement

Because direct torque measurement on a rotating driveshaft is difficult, most monitoring systems use indirect methods, such as measuring cylinder pressure in automotive engines [7], fluid pressure in hydraulic power applications [5], or oil pressure in aircraft engine applications [8]. Contactless methods, typically optical or laser-based with targets affixed to the rotating shaft to enable twist measurements [9-12], tend to provide accurate measurements [13]. However, they rely on clean environments (free of dust, oil mist, and deposited films [3]) and shafts that do not translate axially or laterally. Another option involves shaft-mounted strain gages [14] with rotating frame electronics for data sampling.

This data can be wirelessly transmitted to the fixed frame via battery-powered RF transmitters [15-16] or inductively-powered near-field communication (NFC) systems [17]. Surface acoustic wave (SAW) technology has been used to quantify torque in rotating shafts by measuring the frequency changes of SAW resonators [18]. Unfortunately, wireless technologies such as these depend on MHz range communication frequencies which are notoriously susceptible to the electromagnetic interference (EMI) routinely seen in aerospace qualification testing [19] (i.e. RS103 in MIL-STD-461G). This ultimately leaves them unsuitable for torque feedback in safety-critical aerospace systems.

Direct torque measurement frequently involves magnetostrictive (MS) or variable reluctance (VR) sensors. Magnetostrictive (AKA magnetoelastic) sensors use rings with polarized magnetic fields affixed to a rotating shaft [20]. As these rings are torsionally stressed, they produce magnetic fields that vary with stress; these fields can be measured via solid-state Hall Effect sensors [20]. A unique technological advantage of this approach is its measurement of torsional stress (as opposed to strain), which allows use in applications with small shaft twist angles [21]. MS torque sensing has been used in various automotive applications including feedback for power steering [20] and improved shift control [21]. MS torque sensing has also been implemented on Honeywell's T55 turboshaft engine for the Boeing CH-47 Chinook helicopter [22] and on tiltrotor aircraft quill shafts [23]. Technical challenges include hysteresis from ring-shaft slippage and temperature limitations [20-21].

1.2. Variable Reluctance (VR) Torque Measurement

VR sensors can be used to accurately measure timing differences, twist, and torque between toothed wheels (e.g. gears) as they rotate [24], and are typically hermetically sealed in conductive casings to mitigate vibrational and environmental susceptibility [25-26]. As ferromagnetic gear teeth pass by, changes in magnetic flux produce zero-mean alternating voltage sensor outputs (Figure 1.1).

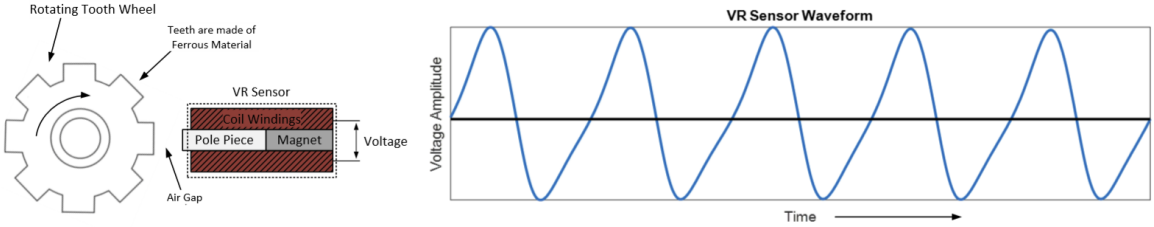

Figure 1.1: Functional schematic of VR sensor (left) and output voltage waveform (right) [27]

For toothed wheels rotating at high speeds, the output voltage is approximately sinusoidal, and the negative-sloped "zero crossings" associated with each tooth passage can be processed as logic level signals for precise timing.

Shaft torque can be calculated from the timing difference between two axially separated VR sensors (Figure 1.2); the resulting twist measurement is proportional to torque via the shaft's torsional stiffness [28-33]. The bandwidth of the torque measurement is tied to the digital filtering used to increase the measurement SNR, typically resulting in a bandwidth containing frequencies between DC and roughly 0.45 times the shaft speed. Axial translation and radial misalignment introduce measurement errors; incorporating a stiff reference shaft

can be used mitigate them [34]. Where space and weight constraints preclude the use of reference shafts, methods have been developed which use arrays of VR sensors to account for radial misalignment [35-36] (Figure 1.2). In one such embodiment, VR sensors are circumferentially distributed over each toothed wheel, making the system tolerant to radial translation.

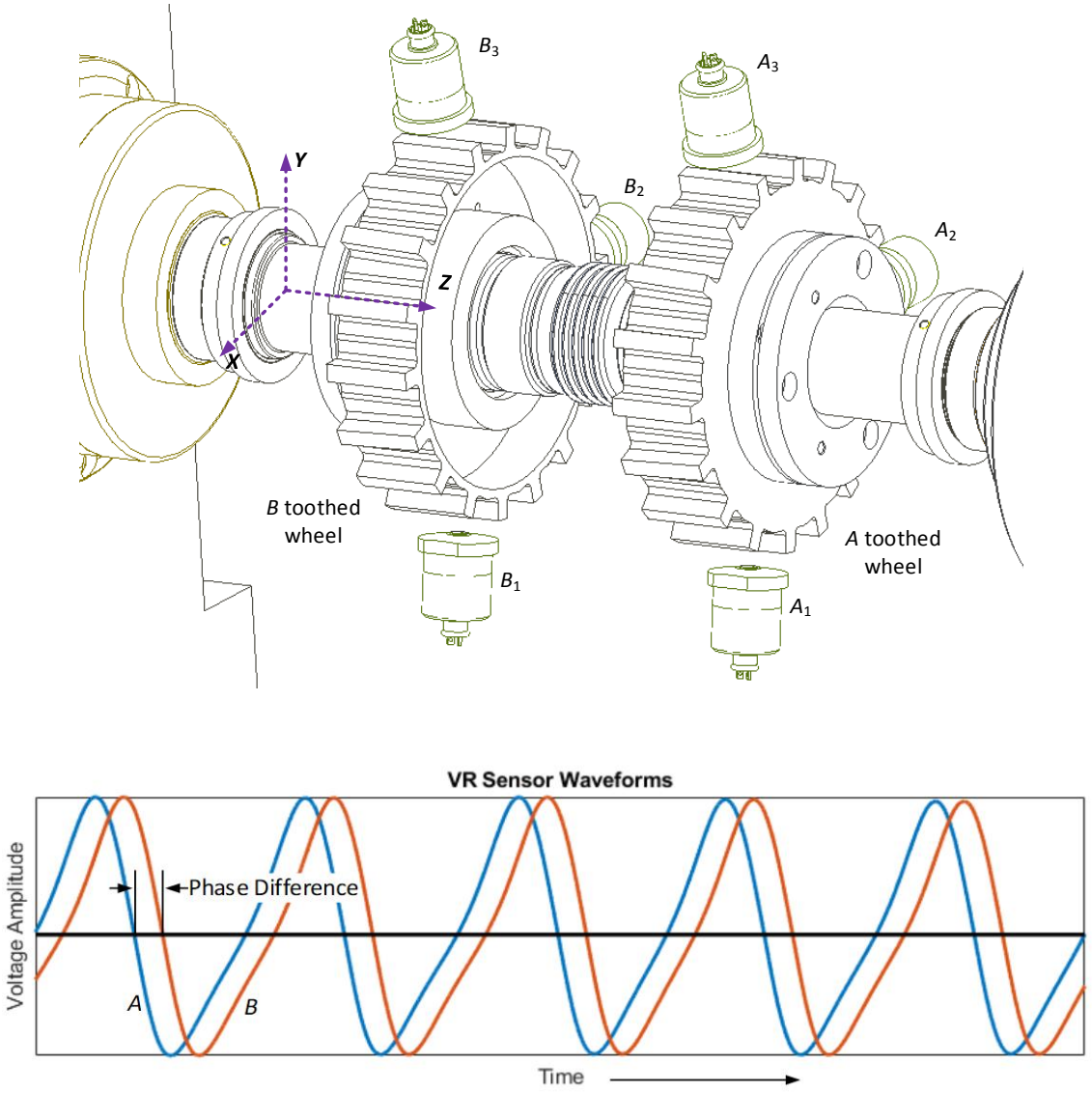

Figure 1.2: Top: Embodiment of VR sensor array measuring two toothed wheels and their relative phasing to determine drivetrain torque, radial misalignment, and axial translation [36]; Bottom: Typical phase difference between two VR sensor waveforms resulting from applied shaft torque.

1.3. Drivetrain Whirl Measurement

VR sensor arrays enable robust and accurate real-time torque monitoring [36], and can be used to distinguish various drivetrain motions including axial and radial translations

and angular misalignments [37]. On aerospace drivetrains, radial misalignment is apparent at the shaft rotational frequency (1P) and its harmonics (2P, 3P, etc.). 1P radial misalignment is usually the significant source of shaft vibration; its measurement can be a good indicator of the rotating machine's health. One manifestation of radial misalignment is shaft whirl, or radial translation perpendicular to a shaft's axis of rotation and synchronous with the shaft's rotational speed (1P). Shaft whirl can be exacerbated by bending moments, flexible bearings, and rotating imbalances; whirl due to these conditions is further compounded when the shaft operates supercritically [38-39]. Figure 1.3 shows a shaft time lapse showing whirl about the shaft's center of rotation.

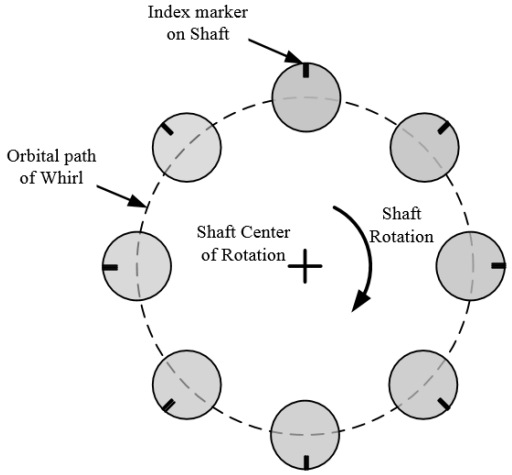

Figure 1.3: Shaft cross-section through time (with index marker) showing rotation along an orbital path [40]

Aircraft engines are one of several applications where shaft whirl is a critical design consideration and operational measurement. Radial misalignment in aircraft engines can occur during maneuver loads, producing radial translation in the engine's turbine and

compressor stages [41]. Other sources of shaft whirl can be attributed to oil-whip in fluid-film bearings [43-45], rotor imbalance driven resonances [46], aerodynamic effects (such as steam whirl [47] or Alford forces [48]), and non-linear rotordynamic phenomena [49]. To prevent catastrophic damage associated with blade strikes, clearance must be provided between the turbine or compressor blade tips and surrounding structures, usually on the order of 10 mils [50]. While increased clearance can reduce the risk of whirl-induced damage, it also reduces the efficiencies of the turbine and compressor stages, resulting in a less efficient engine. For this reason, minimizing radial engine clearance is a conflicting design objective focused on improving efficiency [42].

The analysis of rotordynamic whirl is an active research area [49-51], because reducing engine rotor clearances has significant potential for improved efficiency. One research focus, active clearance control (ACC) systems, has the potential to reduce clearance based on sensor feedback [50, 52]. Another is exploring the use of active magnetic bearings (AMBs) to mitigate the adverse effects of rotordynamic whirl (and maintain adequate engine clearances) via active control schemes [53]. Regardless of the approach, feedback control systems require accurate, real-time whirl information. While proximity sensors are typically used to measure whirl in laboratory or test environments, sensors that can survive permanent installation in harsh aerospace environments are currently unavailable [50]; this is currently a significant impediment to reducing radial engine clearance and increasing efficiency. The VR sensor-based methodology proposed here is an enabling technology, potentially allowing significant increases in aircraft engine efficiency.

Additional benefits of real-time whirl measurement are their potential for health monitoring. In aircraft engines, monitoring gradual increases in whirl amplitude could enable the detection of progressive cracks and the prediction and elimination of blade failures (such as those in Figure 1.4) before they occur. Although the blades aircraft engines are precisely balanced to minimize whirl, small cracks can propagate and gradually shift the blade's center of gravity, resulting in increased whirl amplitude. If measured with the appropriate accuracy, an increase in whirl can be used as a health indicator of an engine's rotating machinery. Several challenges do exist with implementing a VR sensor array to measure whirl in engines: high temperatures in engines necessitate the use of high temperature magnetics and potentially require active cooling of the sensor, high temperature metals such as Inconel and Titanium are not ferrous metals which greatly reduces the voltage output of the VR sensor. Despite these challenges, the real-time estimation of whirl in an aircraft engine would provide crucial measurement information for improvements in engine efficiency and health monitoring.

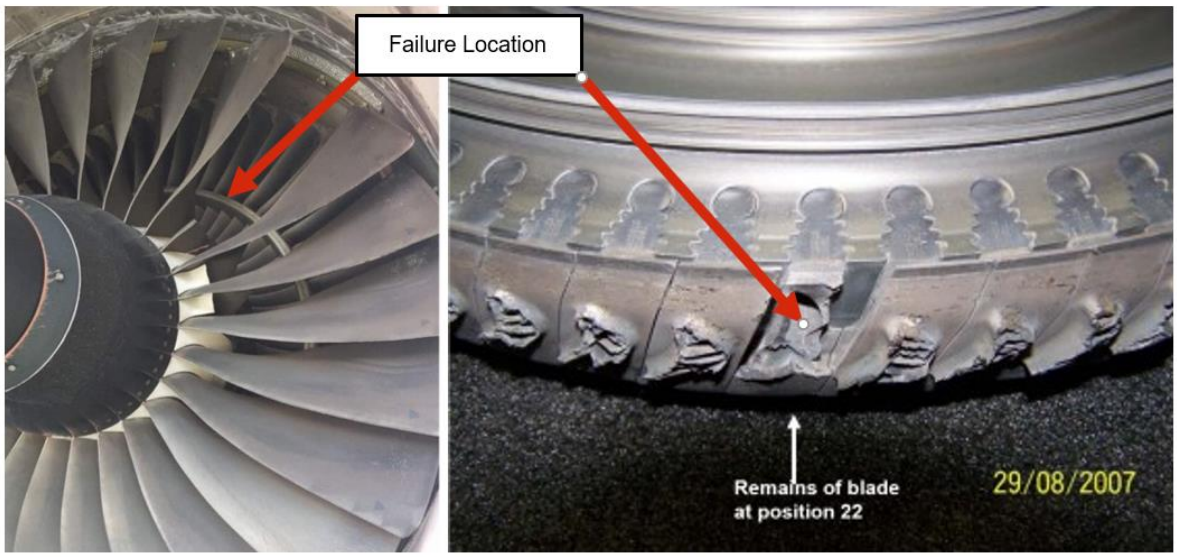

Figure 1.4: Photographs of blade failures on aircraft engines. Left) Missing fan blade on a Rolls Royce Trent 772 engine [54]. Right) Missing high pressure turbine blade on a Rolls Royce BR715 engine [55].

The high-speed, power-transmitting drivetrains of modern aircraft, especially rotary wing aircraft, would benefit from accurate, real-time whirl measurements; such information would enable continuous health monitoring and prevent drivetrain failures between gearboxes [56]. It would also provide indications of typical mechanical issues, such as driveshaft misalignment, and excessive imbalance. Failures in the Airframe Mounted Auxiliary Drive (AMAD) gearbox bearings on the RAAF's F-18 aircraft were traced back to excessive whirl of the input driveshaft [56]. Figure 1.5 shows the location of the AMAD gearbox in the F-18 aircraft (near the engines) which provide power via a high-speed driveshaft. The driveshaft critical speed was found to be slightly above the operating frequency of the driveshaft (greater than 16,000 RPM), causing excessive whirl from gearbox

component imbalances. The resulting vibration caused a failure of the input bearing (Figure 1.6) of the AMAD gearbox resulting in two in-flight fires of RAAF F-18 aircraft [56].

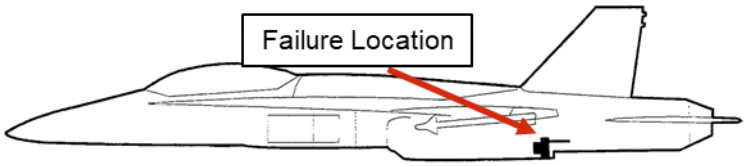

Figure 1.5: Diagram of F-18 AMAD Gearbox location [56]

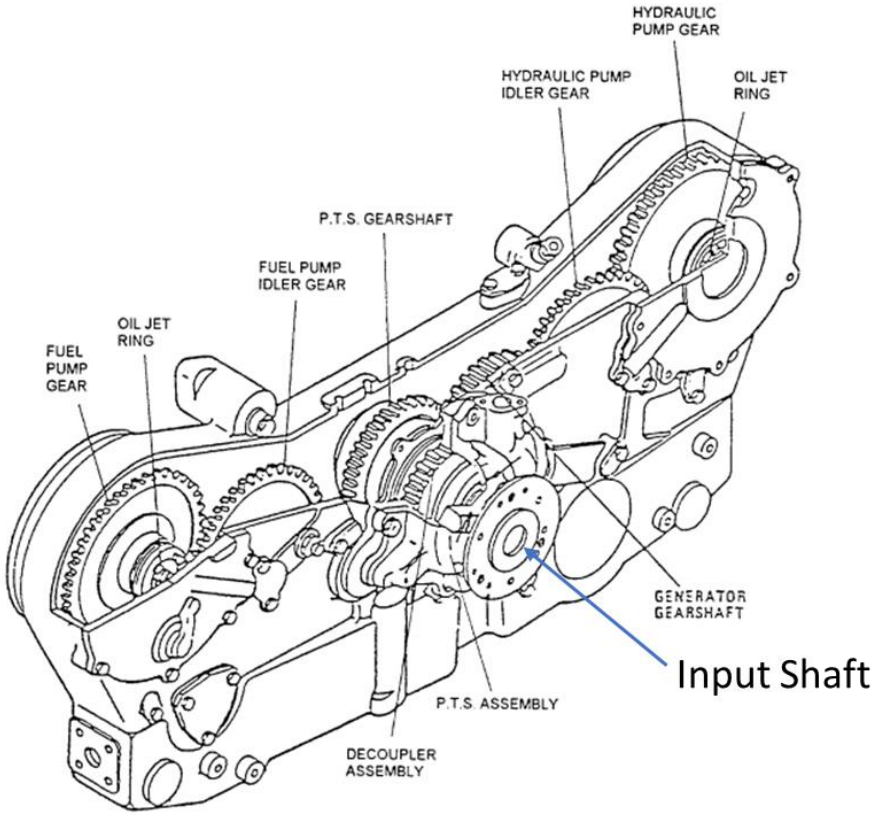

Figure 1.6: Diagram of F-18 AMAD Gearbox containing failed input shaft bearings from excessive whirl [56]

1.4. Jeffcott Rotor Model

The first rotordynamic analysis of high-speed shafts was performed by William Rankine in 1869 [39, 57], though a flaw in his model (where the Coriolis term was neglected) incorrectly predicted unstable operation above the shaft's critical speed [58]. This erroneous conclusion influenced drivetrain design for the next 50 years, where rotors were designed to operate below their critical speed [59, 58]. However, experimental demonstrations of a supercritical steam turbine by De Laval in 1889, coupled with an experimentally observed 2nd critical speed by Kerr in 1916, revealed the flaw in Rankine's analysis [60]. Jeffcott was tasked in 1919 with correcting this discrepancy; Figure 1.7 shows the resulting Jeffcott rotor, a simply-supported shaft with a rotational mass. The low-order linear model associated with this rotor more accurately predicts shaft resonances caused by mass imbalance [51]. In this model, the mass's center of gravity (CG) is offset from the shaft centerline to produce the imbalance excitation.

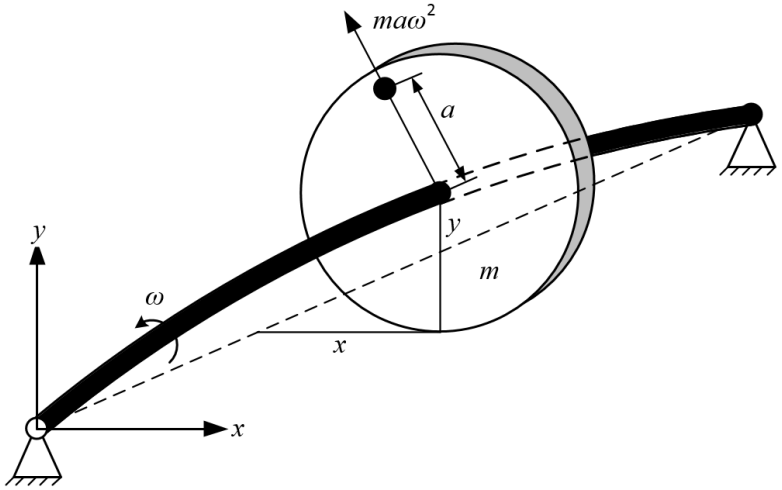

Figure 1.7: Jeffcott rotor diagram [59] showing an inertial mass with an imbalance in the center of a simply supported shaft

While the Jeffcott rotor neglects bearing compliance, it is a valuable tool for predicting the first shaft critical speed, and it successfully predicts stable operation at supercritical speeds. A typical Jeffcott rotor frequency response is shown in Figure 1.8; it clearly possesses the characteristics of a damped second order system. While modern finite element analysis (FEA) tools surpass the Jeffcott rotor model in terms of accuracy, early rotor design used Jeffcott's simple model to provide a theoretical basis for advancing operating speeds past the first critical speed.

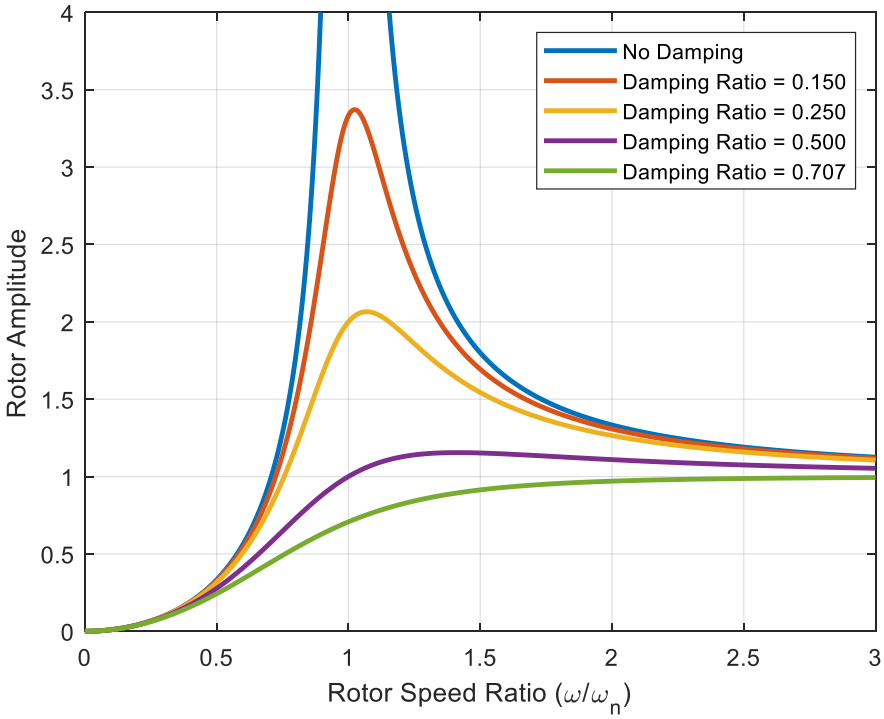

Figure 1.8: Jeffcott rotor amplitude over speed [58]

Chapter 2: Simultaneous Torque and Axial Measurements

For some applications, the measurement of axial shaft loading and displacement is useful for assessing efficiency and health [61-62].Various methods have been developed to measure axial translation [61] and thrust loads [63] in rotating shafts; one novel method for axial translation measurement is to incorporate intermittent slanted teeth on toothed wheels [62]. However, the combined effects of axial translation and slanted teeth create errors in the measurement of torque [62].

This chapter focuses on the development and experimental demonstration of a unique non-contacting VR sensor system that enables simultaneous estimation of torque, speed, and axial translation in high-speed rotating shafts. A novel tooth geometry is introduced featuring alternating slants on every third tooth of an otherwise standard toothed wheel. A novel torque and axial processing (TAP) algorithm allows axial translation to be extracted from the VR sensor measurements. This measurement methodology is detailed, simulated and experimentally validated.

2.1. Methods

To allow simultaneous measurement of shaft torque and axial translation, toothed wheels with a unique alternating slant pattern were integrated into a VR torque monitoring system. This system consists of six VR sensors mounted into a cradle assembly, which encloses the toothed wheels and high-speed rotating shaft (Figure 2.1). The VR cradle

secures two sets of three VR sensors circumferentially spaced at 100° intervals. The shaft has a flexible coupling between the toothed wheels and is driven by a high-speed spindle.

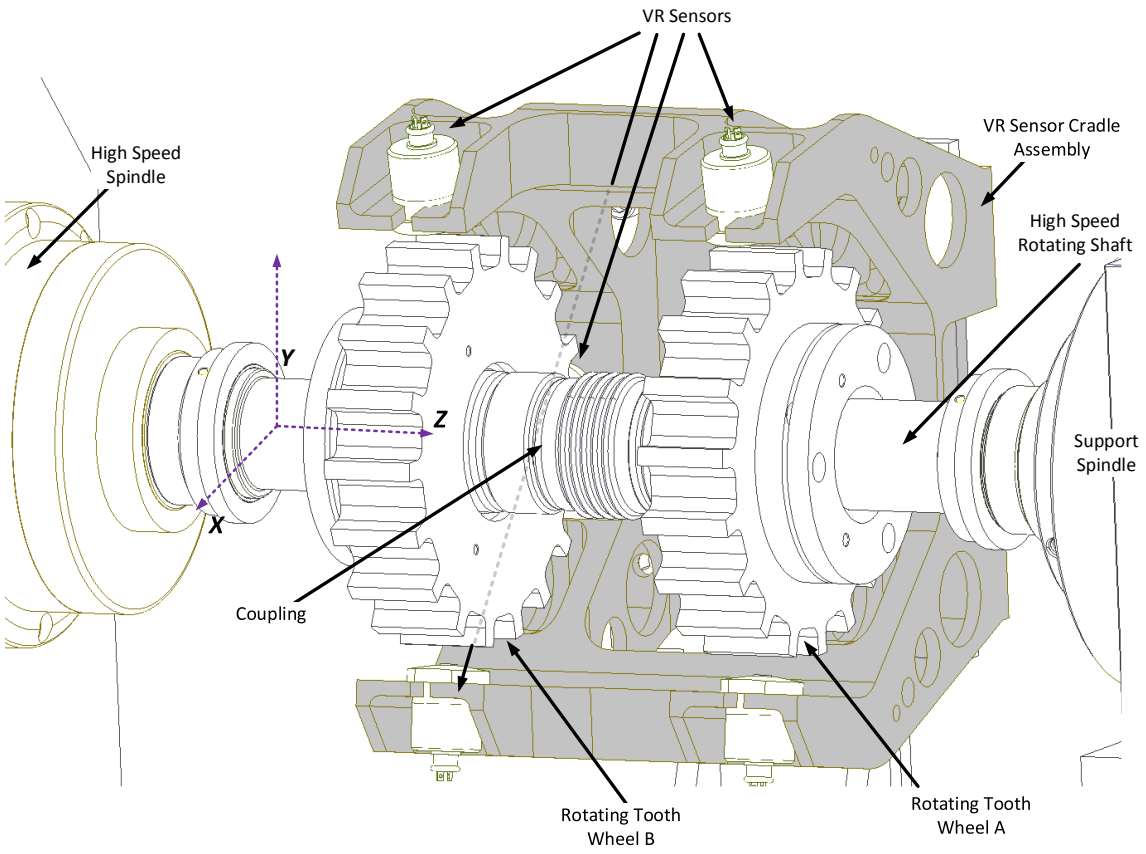

Figure 2.1: Diagram of torque sensing system: cradle with six VR sensors oriented circumferentially around high-speed rotating shaft and flexible coupling with toothed wheels

Each wheel has 18 teeth, with every third tooth having an alternating slant angle of ±2°, so chosen to accommodate typical wheel machining tolerances without adversely affecting the accuracy of torque and radial translation measurements (Figure 2.2).

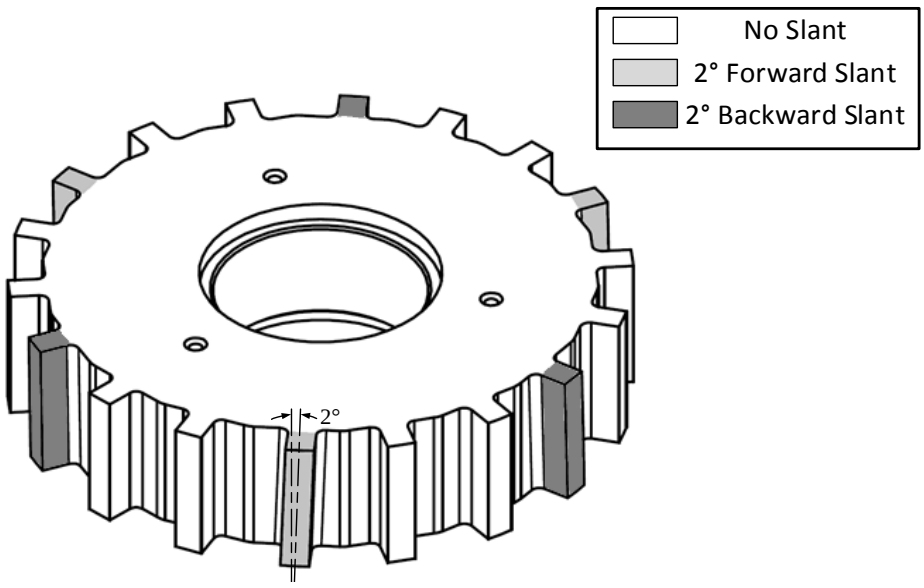

Figure 2.2: Isometric view of toothed wheel with 18 teeth, 12 having no slant, three with a 2° forward slant, and three with a 2° backward slant.

Each toothed wheel is identical to within machining tolerances; wheel *A* is located on the support spindle side and wheel *B* is located on the high-speed spindle drive side. The three sensors oriented around wheel *A* are designated A_1-A_3; the sensors oriented around wheel *B* are designated B_1-B_3 (Figure 2.3).

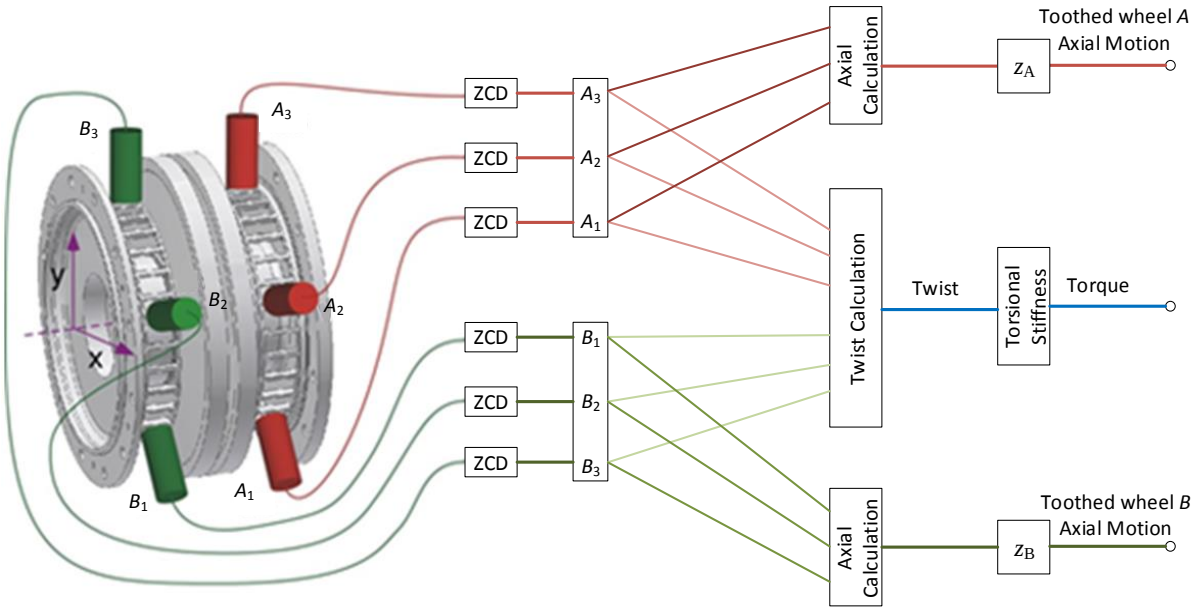

Figure 2.3: Schematic of torque measurement system and processing with VR sensor Zero-Cross Detections (ZCD) and TAP Algorithm

As each tooth passes a sensor, a voltage pulse is generated, and a logic signal is produced based on the zero crossings of this voltage (Figure 2.4). On the falling edge of this signal, a timing value is acquired at each zero crossing and used in the TAP algorithm processing:

$$\vec{v}^{k} = \left[v_{A_1}^{k} \quad v_{A_2}^{k} \quad v_{A_3}^{k} \quad v_{B_1}^{k} \quad v_{B_2}^{k} \quad v_{B_3}^{k} \right]^{T} \tag{1}$$

Where v_i^k indicates the k^{th} zero-crossing time (in microcontroller clock cycles) of the i^{th} sensor.

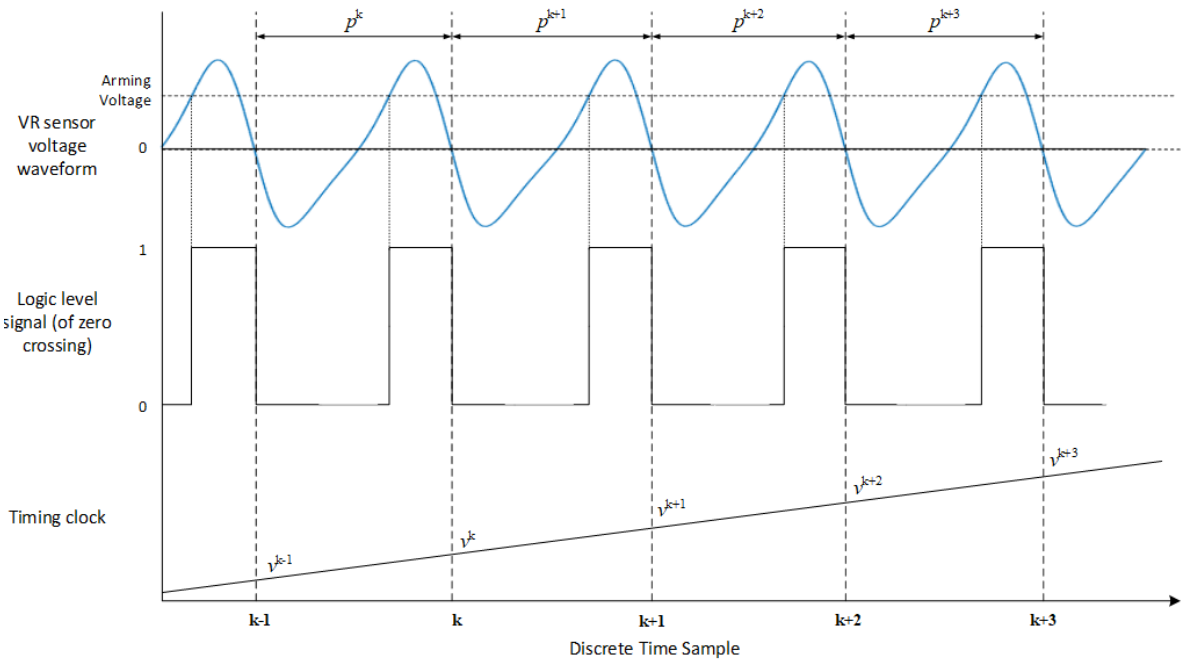

Figure 2.4: VR sensor conditioning schematic: voltage waveform with arming voltage threshold, zero-crossing logic level signal with tooth period p^k, and timing clock to capture zero-crossing logic signals

Each sensor's tooth period p_i^k is simply the time between successive zero crossings:

$$\vec{p}^{\,k} = \begin{bmatrix} p_{A_1}^k \\ p_{A_2}^k \\ p_{A_3}^k \\ p_{B_1}^k \\ p_{B_2}^k \\ p_{B_3}^k \end{bmatrix} = \begin{bmatrix} v_{A_1}^k - v_{A_1}^{k-1} \\ v_{A_2}^k - v_{A_2}^{k-1} \\ v_{A_3}^k - v_{A_3}^{k-1} \\ v_{B_1}^k - v_{B_1}^{k-1} \\ v_{B_2}^k - v_{B_2}^{k-1} \\ v_{B_3}^k - v_{B_3}^{k-1} \end{bmatrix} \tag{2}$$

2.1.1. Signal Processing

The TAP algorithm enables real-time calculation of shaft speed, axial translation, and shaft torque based on the zero-crossing time vector $\vec{v}^{k}$. For each VR sensor, *N* successive tooth periods P_i^k can be averaged and filtered to quantify the wheel's period P^k (in timing clock cycles) according to the TAP filtering schematic of Figure 2.5.

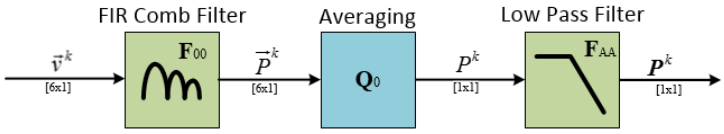

Figure 2.5: TAP filtering schematic to determine clock cycles per revolution

The FIR comb filter $\boldsymbol{F}_{00}$ removes noise and the effects of machining tolerances from the zero-crossings and calculates each sensor's "period of revolution" or P_i^k:

$$P_i^k = p_i^k + p_i^{k-1} + \ldots + p_i^{k-N+2} + p_i^{k-N+1} = \sum_{n=0}^{N-1} p_i^k z^{-n} = \boldsymbol{F}_{00} v_i^k \tag{3}$$

where *N* is the wheel's number of teeth and z^{-n} is the unit delay function. Additional accuracy is achieved by averaging across all sensors. A low-pass filter $\boldsymbol{F}_{AA}$, in this case a 2nd Order Butterworth filter, is used to eliminate aliasing in the measurement data which is transmitted at rates on the order of 50 to 100 Hz.

$$\boldsymbol{P}^k = \boldsymbol{F}_{AA} P^k = \boldsymbol{F}_{AA} \frac{1}{6} \left(\sum_{i=1}^{6} P_i^k \right) = \boldsymbol{F}_{AA} \boldsymbol{Q}_0 \vec{P}^k \tag{4}$$

The resulting timing clock cycles per revolution ($\boldsymbol{P}^k$) can be used to determine shaft speed f_{shaft}^k:

$$f_{\text{shaft}}^k = \frac{f_{\text{clock}}}{\boldsymbol{P}^k} \tag{5}$$

where f_{clock} is the timing clock speed in Hz and f_{shaft}^k is the shaft speed, also in Hz. The TAP algorithm also calculates axial shaft translation, as shown in the filtering schematic of Figure 2.6.

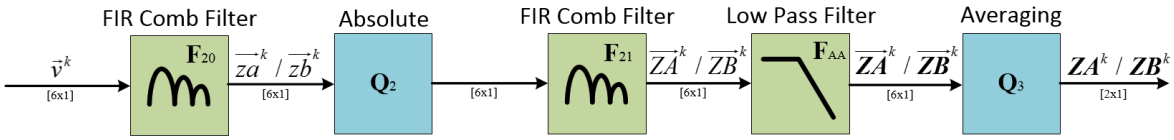

Figure 2.6: Filtering schematic to determine axial translation

Recalling that every third tooth is slanted (Figure 2.2), the effects of tooth slant can be isolated by applying an FIR comb filter $\boldsymbol{F}_{20}$ which extracts 3/Rev content:

$$\boldsymbol{F}_{20} = \frac{3}{N}\sum_{n=0}^{N/3-1}(-1)^n(z^{-3n} - z^{-3n-1}) \tag{6}$$

The alternating negative sign accounts for the alternating directions of tooth slant. The FIR comb filter $\boldsymbol{F}_{20}$ can be applied to each sensor's zero-crossing time v_i^k and the absolute values can be calculated:

$$\left|za_i^k\right| = \left|\boldsymbol{F}_{20}v_i^k\right| = \boldsymbol{Q}_2\boldsymbol{F}_{20}v_i^k \qquad \text{where i = 1 to 3} \tag{7}$$

$$\left|zb_i^k\right| = \left|\boldsymbol{F}_{20} v_i^k\right| = \boldsymbol{Q}_2 \boldsymbol{F}_{20} v_i^k \quad \text{where i = 4 to 6} \tag{8}$$

Applying an additional FIR filter $\boldsymbol{F}_{21}$ to $\left|za_i^k\right|$ and $\left|zb_i^k\right|$ and applying anti-alias filtering for transmission, calculates an intermediate result of each wheel's axial translation. Because axial translation is theoretically identical at each of the three sensor locations for a given toothed wheel (*A* or *B*), these values can be averaged:

$$\boldsymbol{ZA}^k = \frac{1}{3}\sum_{i=1}^{i=3} \boldsymbol{ZA}_i^k = \boldsymbol{Q}_3 \boldsymbol{F}_{AA} ZA_i^k = \boldsymbol{Q}_3 \boldsymbol{F}_{AA} \frac{\left(1 + z^{-1} + z^{-2}\right)}{3} \left|za_i^k\right| = \boldsymbol{Q}_3 \boldsymbol{F}_{AA} \boldsymbol{F}_{21} \left|za_i^k\right| \tag{9}$$

$$\boldsymbol{ZB}^k = \frac{1}{3}\sum_{i=4}^{i=6} \boldsymbol{ZB}_i^k = \boldsymbol{Q}_3 \boldsymbol{F}_{AA} ZB_i^k = \boldsymbol{Q}_3 \boldsymbol{F}_{AA} \frac{\left(1 + z^{-1} + z^{-2}\right)}{3} \left|zb_i^k\right| = \boldsymbol{Q}_3 \boldsymbol{F}_{AA} \boldsymbol{F}_{21} \left|zb_i^k\right| \tag{10}$$

Note that the $\boldsymbol{ZA}^k$ value corresponds to the *A* toothed wheel, and the $\boldsymbol{ZB}^k$ value corresponds to the *B* toothed wheel. The $\boldsymbol{ZA}^k$ value and $\boldsymbol{ZB}^k$ value can be correlated to axial translations.

$$z_A^k = \frac{3}{2} \frac{2\pi R_A}{\tan(\beta)} \frac{f_{\text{shaft}}^k}{f_{\text{clock}}} \boldsymbol{ZA}^k \tag{11}$$

$$z_B^k = \frac{3}{2} \frac{2\pi R_B}{\tan(\beta)} \frac{f_{\text{shaft}}^k}{f_{\text{clock}}} \boldsymbol{ZB}^k \tag{12}$$

Where z_A^k and z_B^k corresponds to the axial translation of the *A* and *B* toothed wheels respectively, R_A is the *A* toothed wheel radius, R_B is the *B* toothed wheel radius, and β is the angle of the slanted teeth. The TAP algorithm uses phase differences between wheel *A* and *B* zero crossings (Figure 1.2), which are indications of shaft twist $\Delta\theta$, and which are directly related to torque *T* [64]:

$$\Delta\theta = \frac{TL}{GJ} \equiv \frac{1}{K}T \tag{13}$$

where T is torque, L is the axial length between each toothed wheel, G is the shear modulus, J is the polar moment of inertia, and K is the shaft's torsional stiffness. Shaft twist can be determined according to the filtering schematic of Figure 2.7.

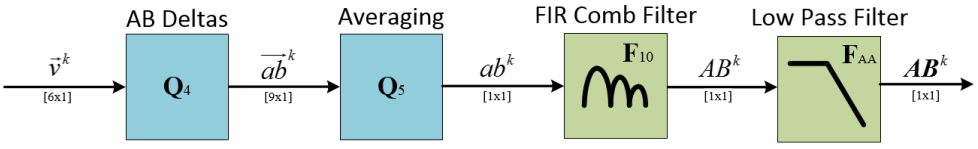

Figure 2.7: Filtering schematic to determine twist

The phase measurement vector $\overrightarrow{ab}^k$ quantifies phase differences between sensors on the A toothed wheel and the B toothed wheel:

$$\overrightarrow{ab}^k = \begin{bmatrix} v_{A_1}^k - v_{B_1}^k \\ v_{A_1}^k - v_{B_2}^k \\ v_{A_1}^k - v_{B_3}^k \\ v_{A_2}^k - v_{B_1}^k \\ v_{A_2}^k - v_{B_2}^k \\ v_{A_2}^k - v_{B_3}^k \\ v_{A_3}^k - v_{B_1}^k \\ v_{A_3}^k - v_{B_2}^k \\ v_{A_3}^k - v_{B_3}^k \end{bmatrix} = \mathbf{Q}_4 \vec{v}^k \tag{14}$$

Each element of this phase measurement vector contributes equally to a measure of twist, so these measurements can be averaged into a single-phase measurement ab^k. A FIR digital comb filter $\boldsymbol{F}_{10}$ can be applied to ab^k to remove noise and the effects of machining defects in the twist calculation. Applying a low pass anti-aliasing filter $\boldsymbol{F}_{AA}$ eliminates aliasing in the transmitted measurements.

$$\boldsymbol{AB}^k = \boldsymbol{F}_{AA} AB^k = \boldsymbol{F}_{AA} \sum_{n=0}^{n=N-1} \frac{z^{-n} ab^k}{N} = \boldsymbol{F}_{AA}\boldsymbol{F}_{10} ab^k = \boldsymbol{F}_{AA}\boldsymbol{F}_{10} \sum_{j=1}^{j=9} \frac{ab_j^k}{9} = \boldsymbol{F}_{AA}\boldsymbol{F}_{10}\boldsymbol{Q}_5 \overrightarrow{ab}^k \tag{15}$$

The $\boldsymbol{AB}^k$ value can be correlated to shaft twist between toothed wheels *A* and *B*:

$$\Delta\theta^k = 2\pi \frac{f_{\text{shaft}}^k}{f_{\text{clock}}} \boldsymbol{AB}^k \tag{16}$$

where $\Delta\theta^k$ is the shaft twist (in radians) between the *A* and *B* toothed wheels. The shaft twist can be related to shaft torque *T* via (13).

$$T = K(\Delta\theta) = \frac{GJ}{L}\Delta\theta \tag{17}$$

2.1.2. Computer simulations

The performance of this TAP algorithm in estimating shaft speed, torque and axial translation can be evaluated via numerical computer simulations. Given the geometrical properties of each toothed wheel (*N*: number of teeth on wheel, *R*: radius of wheel, and $\pm\beta$: the slant angle of every third tooth) and the mechanical properties of the shaft (*L*: its length, *J*: its polar moment of inertia, and *G*: its shear modulus), zero-crossing timing vectors $\vec{v}^k$ can be simulated for a variety of shaft speeds f_{shaft}^k and applied torque *T*:

$$\vec{v}^{k} = \frac{f_{clock}}{N} \int_{k'=0}^{k'=k} \frac{dk'}{f_{\text{shaft}}^{k'}} + \frac{f_{\text{clock}}}{f_{\text{shaft}}^{k}} \begin{bmatrix} \theta_A^k / 2\pi + \tan(\beta^k) z^k / 2\pi R_A \\ \theta_A^k / 2\pi + \tan(\beta^k) z^k / 2\pi R_A \\ \theta_A^k / 2\pi + \tan(\beta^k) z^k / 2\pi R_A \\ \theta_B^k / 2\pi + \tan(\beta^k) z^k / 2\pi R_B \\ \theta_B^k / 2\pi + \tan(\beta^k) z^k / 2\pi R_B \\ \theta_B^k / 2\pi + \tan(\beta^k) z^k / 2\pi R_B \end{bmatrix} \tag{18}$$

Each toothed wheel (*A* and *B*) is assumed to have the same axial translation, denoted by z^k. The shaft twist $\Delta\theta^k$ is related to the angular displacement of each toothed wheel and shaft torque by:

$$\Delta\theta^k = \theta_A^k - \theta_B^k = \frac{T^k}{K} \tag{19}$$

Equation (18) can be used to estimate the zero-crossing timing vector $\vec{v}^{\,k}$. Using MATLAB 2017a, timing vectors were simulated over 30 seconds for two cases: 1. constant axial position, variable shaft speed, and torque; 2. variable shaft speed, variable torque, and varying axial translation. Table 2.1 summarizes the simulation parameters for both cases.

Table 2.1: Simulation parameters and geometric constants

Parameter	Variable	Value
Radius of *A* toothed wheel	R_A	2.179 [in]
Radius of *B* toothed wheel	R_B	2.179 [in]
Number of teeth	N	18
Clock speed of measurement	f_{clock}	200 [MHz]
Angle of slanted teeth	β	2 [°]
Torsional stiffness of driveshaft	K	50 [ft-lbs/°]
Anti-aliasing filter order	n	2
Anti-aliasing filter cutoff	f_b	133.3 [Hz]

2.1.2.1.Simulation 1: Constant axial position, variable speed and torque

The first simulation analyzed typical capabilities of a VR torque measurement system: a shaft rotating with fixed axial position, but with prescribed speed and torque profiles. Table 2.2 details the simulation profiles.

Table 2.2: Axial position, rotational speed, and torque profiles used in Simulation 1

Axial position [in]	z	Shaft Speed [RPM]	f_{shaft}	Torque [ft-lbs]	T	Time [sec]
0.30		8000.0		0.25		$0.0 \leq t \leq 7.5$
		$8000.0 - 50.0(t - 7.5)/2.5$		$0.25 + 0.75(t - 7.5)/2.5$		$7.5 < t \leq 10.0$
		7950.0		1.00		$10.0 < t \leq 15.0$
		$7950.0 - 50.0(t - 15.0)/2.5$		$1.0 + 0.65(t - 15.0)/2.5$		$15.0 < t \leq 17.5$
		7900.0		1.65		$17.5 < t \leq 22.5$
		$7900.0 + 100.0(t - 22.5)/2.5$		$1.65 - 1.4(t - 22.5)/2.5$		$22.5 < t \leq 25.0$
		8000.0		0.25		$25.0 < t \leq 30.0$

2.1.2.2.Simulation 2: Variable axial position, torque, and speed

The second simulation tested more advanced capabilities of the TAP algorithm by considering variable axial position during prescribed speed and torque profiles. Table 2.3 details the simulation profiles. In practice, axial translations of a drivetrain are driven by

maneuver loads on an aircraft typically at a bandwidth below 5 Hz. A 20 Hz axial translation input was used in Simulation 2 to demonstrate the TAP algorithm's ability to measure any axial translation resulting from aircraft maneuver loads.

Table 2.3: Axial position, rotational speed and torque profiles used in Simulation 2

Axial position [in]	z	**Shaft Speed [RPM]**	f_{shaft}	**Torque [ft-lbs]**	T	**Time [sec]**
0.30		8000.0		0.25		$0.0 \leq t \leq 2.5$
$0.30 + 0.1\ sin(2\pi\ 20\ t)$		8000.0		0.25		$2.5 < t \leq 7.5$
		$8000.0 - 50.0(t - 7.5)/2.5$		$0.25 + 0.75(t - 7.5)/2.5$		$7.5 < t \leq 10.0$
		7950.0		1.0		$10.0 < t \leq 15.0$
		$7950.0 - 50.0(t - 15.0)/2.5$		$1.00 + 0.65(t - 15.0)/2.5$		$15.0 < t \leq 17.5$
		7900.0		1.65		$17.5 < t \leq 22.5$
0.30		$7900.0 + 100.0(t - 22.5)/2.5$		$1.65 - 1.4(t - 22.5)/2.5$		$22.5 < t \leq 25.0$
		8000.0		0.25		$25.0 < t \leq 30.0$

2.1.3. Experimental Testing

To experimentally validate the TAP algorithm's torque and axial translation measurement capabilities, a laboratory test rig capable of rotating the shaft and toothed wheels at high speeds, while simultaneously applying prescribed torque and axial displacement, was constructed (Figure 2.8). This test rig consisted of a high-speed machine tool spindle (Fischer MFM-1224/24, Racine, WI) driving a 30mm diameter steel shaft with a flexible coupling (GAM, KHS-15, Mt. Prospect, IL) between two toothed wheels. An electromagnetic (eddy-current) brake (Magtrol BHB-6B, Buffalo, NY) was used to apply torque, which was measured using a reference transducer (Magtrol TM 307/011, Buffalo, NY). Two magnetic encoders (Lika SMRI5-L-1-32-N-L10-J, Columbus, OH) and their corresponding magnetic rings (Lika MRI/48C-32-5-35, Columbus, OH) were incorporated to measure reference twist.

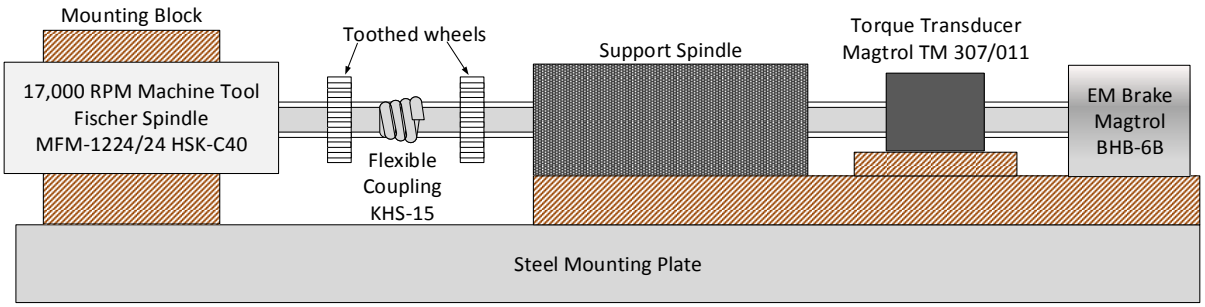

(a)

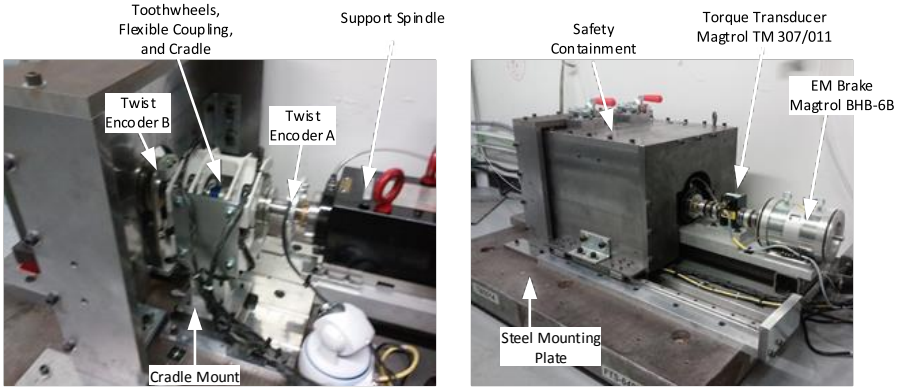

(b) (c)

Figure 2.8: Experimental test rig: a) Block diagram of experimental test rig b) Photograph of the left portion of the test rig showing high speed spindle, toothed wheels, cradle, coupling, and support spindle c) Photograph of the right portion showing the support spindle, the torque transducer, electromagnetic brake, and steel mounting plate

This spindle enabled testing at realistic rotational speeds of up to 17,000 RPM. The flexible coupling was sized to ensure that the spindle torque produced measurable twist (~0.05°) between the two toothed wheels. To establish the nominal coupling stiffness, preliminary tests were run with various torques and it was determined to be 49.31 ft-lbs. A photograph of the experimental cradle setup is shown in Figure 2.9.

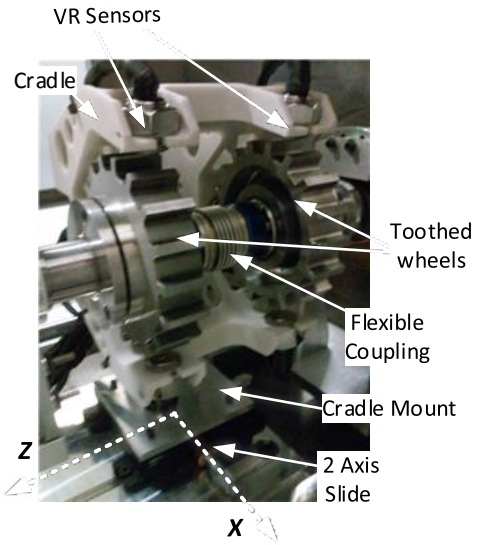

Figure 2.9: Photograph of VR sensor cradle

The cradle and its associated mounting brackets were attached to a two-axis micrometer slide (Figure 2.9), which allowed axial translation to be simulated by moving the cradle in the *z* direction. This enabled precise displacements as small as 0.001" that could be correlated to sensor measurements. All high-speed, high-energy drivetrain components were contained in within a ¾" steel enclosure for safety, as parts rotating at these speeds posed a significant safety risk if mechanical failure occurred. The six VR sensor outputs were transmitted via shielded cables to customized signal processing hardware (Figure 2.10).

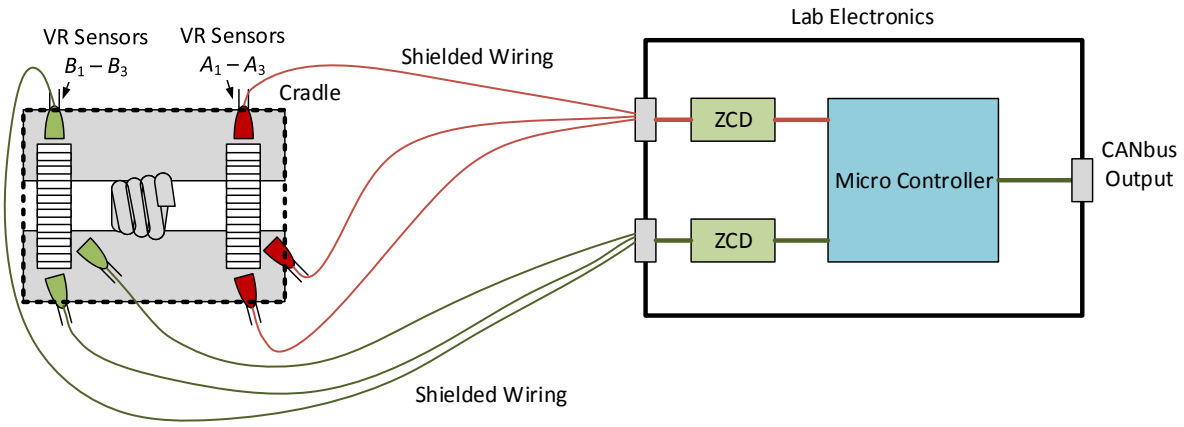

Figure 2.10: Schematic of sensor wiring to processing electronics

VR sensor zero-crossing detection (ZCD) was implemented using an integrated circuit designed specifically for this purpose. The resulting digital signal was routed to a dual-core 200 MHz microcontroller (Texas Instruments LAUNCHXL-F28379D) for real-time filtering and calculation. TAP algorithm results were output to a CANbus for data recording purposes.

2.1.3.1.Experimental calibration

Preliminary testing was conducted to calibrate the experimental setup and TAP algorithm. During these tests, the toothed wheels were precisely aligned with the cradle sensors. Feeler gauges were used to measure a gap of roughly 0.190" between sensors and teeth (Figure 2.11); this required setting the horizontal slide position of the two-axis slide's x-axis to 0.138". Torque and axial position were recorded via CANbus at an 83 Hz sample rate. Because the TAP algorithm relies on measurements that can change significantly with temperature, testing was conducted over short intervals to minimize temperature variations. Table 2.4 summarizes the experimental parameters.

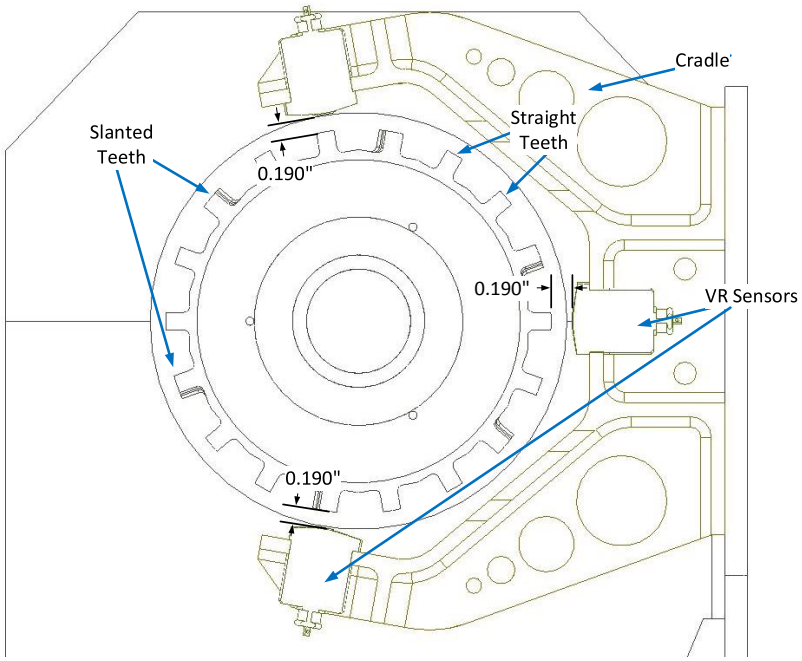

Figure 2.11: Schematic of centered cradle and toothed wheels

Table 2.4: Experimental parameters

Parameter	Variable	Value
Radius of *A* toothed wheel	R_A	2.179 [in]
Radius of *B* toothed wheel	R_B	2.179 [in]
Number of teeth	N	18
Clock speed of measurement	f_{clock}	200 [MHz]
Shaft rotational speed	f_{shaft}	8000 [RPM]
Angle of slanted teeth	B	2 [°]
Horizontal slide position	x	0.138 [in]
Anti-aliasing filter order	n	2
Anti-aliasing filter cutoff	f_b	15 [Hz]

Axial position calibration was performed by adjusting the two-axis slide's micrometer dial (Figure 2.9) while the shaft was stopped, and then rotating up to 8,000 RPM with no applied torque. This process was repeated while the dial was adjusted in 0.025" increments

from 0.000" to 0.500", which resulted in 21 discrete measurements. The axial position estimates from calibration testing are presented in Figure 2.12.

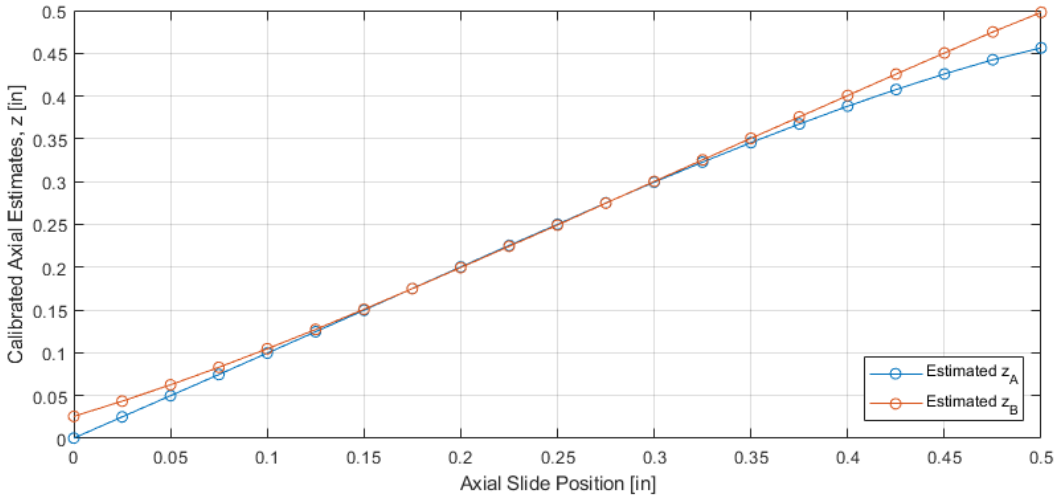

Figure 2.12: Calibrated axial estimates from preliminary testing showing approximately linear trends with axial slide position.

Non-linear trends above 0.30" for the z_A estimate and below 0.15" for the z_B estimate reveal the limits of each sensor's measurement range. More specifically, these non-linearities arise as each VR sensor nears the edge of its corresponding toothed wheel. Preliminary testing also revealed a small bias torque which varied with axial position, even without the Magtrol BHB-6B brake energized. This bias torque is believed to result from slight misalignment between the axial slide and the centerline of the driveshaft, and possibly machining tolerances in the wheel teeth.

2.1.3.2.Experiment 1: Constant axial position, variable speed, and torque

First, drivetrain torque was varied, while axial position was fixed, by actuating the electromagnetic brake in a ramp-wise fashion (Figure 2.13, Table 2.5) so that torque ranged from T_0 (the test stand's nominal drag torque) to 1.6 ft-lbs, corresponding to twist variations from 0 to 0.05 degrees. For these tests, axial position was maintained constant at the midpoint of its axial range (0.250").

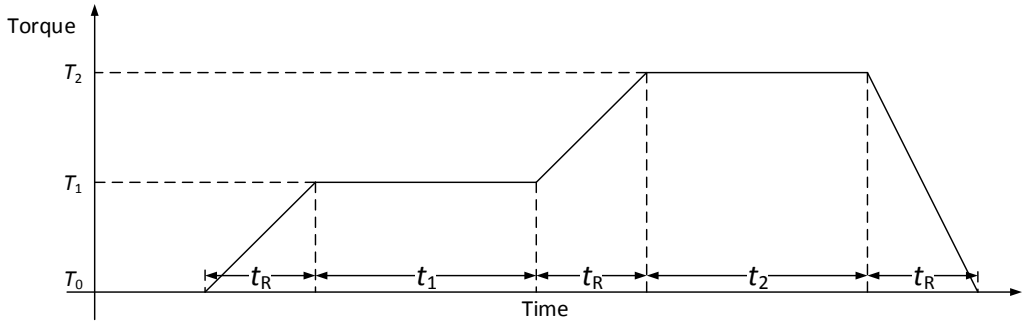

Figure 2.13: Test Case 1 variable torque profile

Table 2.5: Ramp profile parameters for Experiment 1

Parameter	Symbol	Value
Ramp time	t_R	2 [sec]
Dwell time at torques	t_1, t_2	5 [sec]
Drag torque	T_0	0.25 [ft-lbs]
First torque	T_1	1.0 [ft-lbs]
Second torque	T_2	1.6 [ft-lbs]

2.1.3.3.Experiment 2: Variable axial position, torque and speed

Next, torque and axial position were varied simultaneously. The applied torque profile was a ramp pattern identical to Figure 2.13, Table 2.5. Axial position was varied by pulling

against the two-axis slide's spring loading mechanism, moving the sensor cradle, resulting in an approximate axial stroke of 0.20" to 0.35" performed external to the safety enclosure.

2.2. Results

2.2.1. Simulation Results

A comparison of estimated and actual shaft speed and torque for Simulation 1, with fixed axial position, is shown in Figure 2.14. The delay-corrected errors deviate by less than 0.5 RPM and 0.005 ft-lbs, respectively.

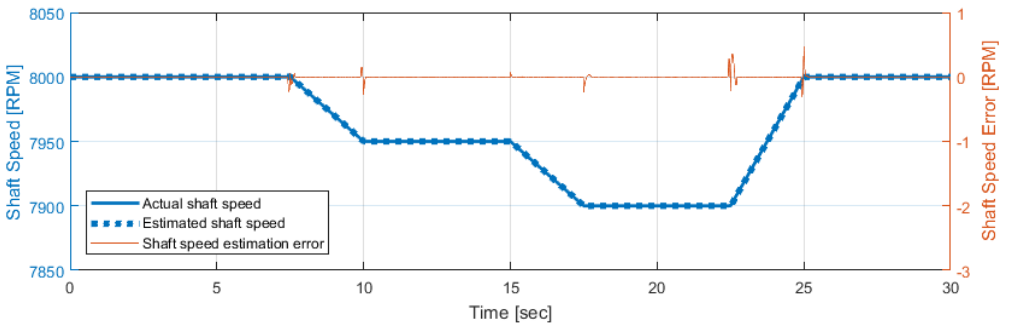

(a)

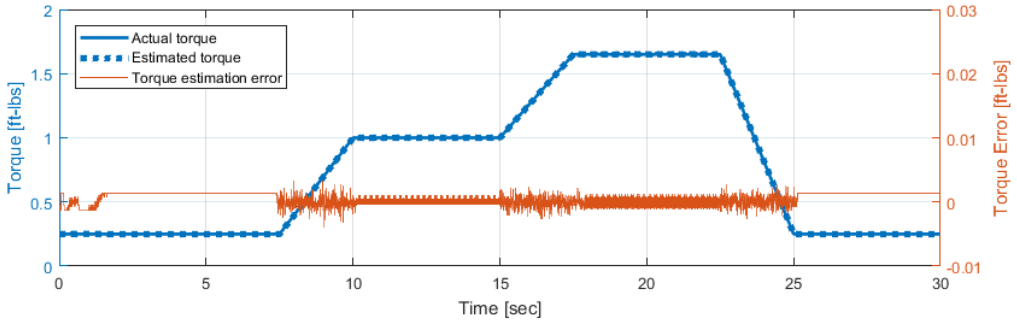

(b)

Figure 2.14: Simulation 1 results for fixed axial position, variable speed and torque: (a) estimated and actual shaft speed and error; (b) estimated and actual torque and error showing noise mainly from quantization.

A comparison of estimated and actual shaft speed and torque for Simulation 2, where shaft speed, torque and axial translation were all varied, is presented in Figure 2.15. TAP-estimated shaft speed and torque are indistinguishable from the actual (simulated) profiles, with estimation errors below 0.5 RPM and 0.005 ft-lbs, respectively. TAP-computed axial position is also indistinguishable from the actual profile. The phase-lag corrected axial position error during steady state conditions was negligible (less than 0.0001 inch) and during the sinusoidal motion was less than 0.004 inches.

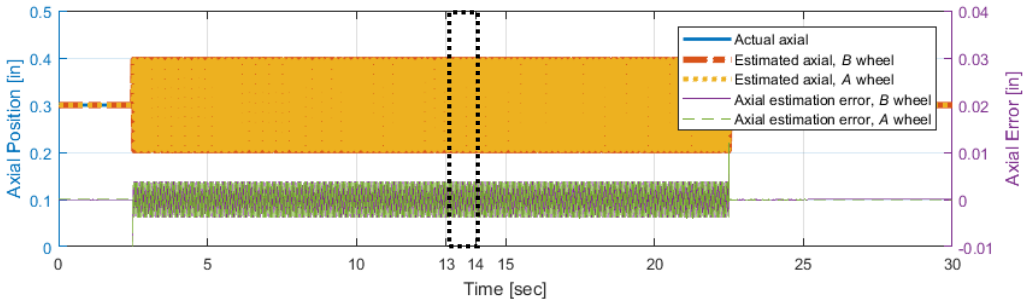

(a)

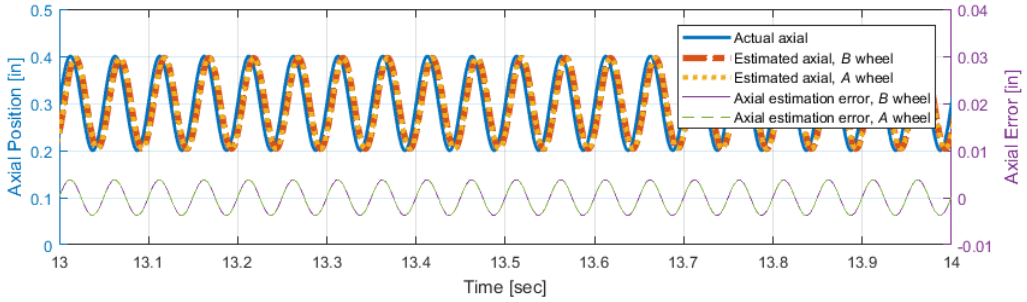

(b)

Figure 2.15: Simulation 2 results showing estimated axial position on both toothed wheels: a) profile throughout entire simulation b) during sinusoidal axial translation

The slanted tooth pattern produced harmonics of the shaft rotational frequency, which are evident in the resonant peaks of Figure 2.16a. The amplitudes of these harmonics, which are a result of axial translation, can be isolated by applying a 3/Rev pass filter $\boldsymbol{F}_{20}$ as defined by (7) to the tooth period shown in Figure 18b. After processing $za^{k}_{A_1}$ according to (7) through (10), the frequency content shifted as shown in Figure 18c. Because $za^{k}_{A_1}$ is an alternating 3/Rev signal, taking the absolute value $\boldsymbol{Q}_2$ shifts the frequency content to 0/Rev and 6/Rev, and applying a 3-sample moving average $\boldsymbol{F}_{21}$ removes the 6/Rev content as shown in Figure 2.16c. The result is then filtered as shown in Figure 2.16d, averaged, and speed-normalized as detailed in (7) through (12). The calculated axial translation approximates the 20 Hz content and is

indistinguishable from the simulation input. However, due to the resonant peak at 3/Rev, the TAP algorithm's digital filtering must eliminate axial translation effects from shaft speed and torque calculations.

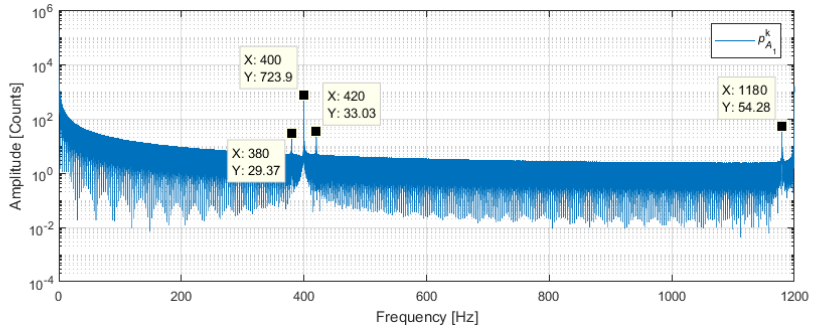

(a)

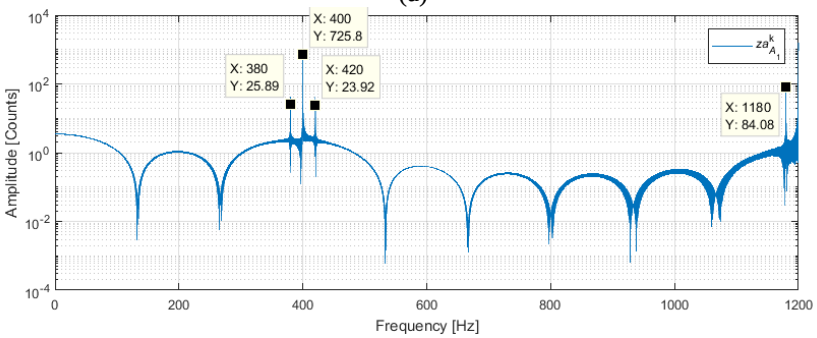

(b)

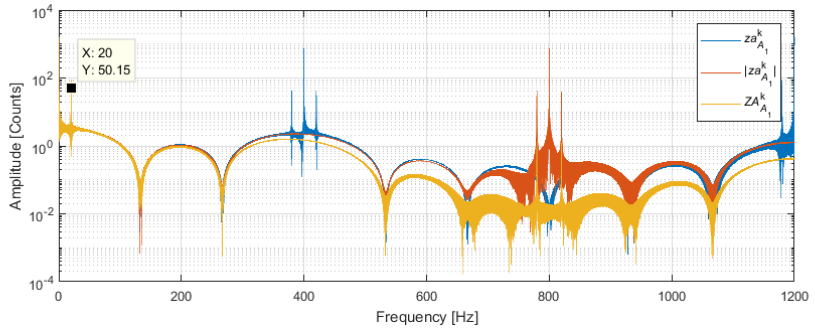

(c)

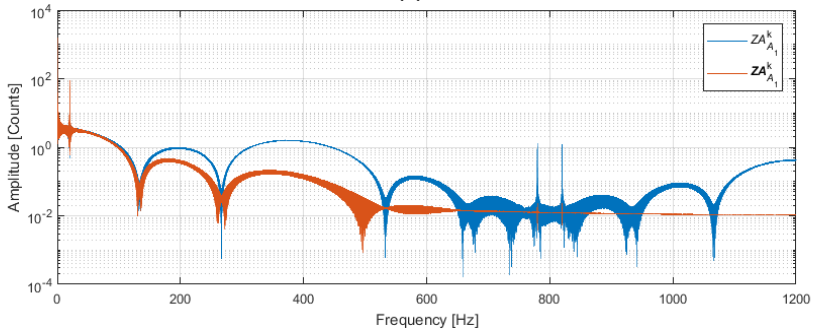

(d)

Figure 2.16: Simulation 2 results showing the progression of TAP filtering: a) FFT of A_1 sensor tooth period p^k , showing a resonant peak at 3/Rev with beating responses at 380 Hz and 420 Hz b) Application of $\boldsymbol{F_{20}}$ to isolate 3/Rev content c) Absolute value operation $\boldsymbol{Q_2}$ applied to rectify 3/Rev content and application of $\boldsymbol{F_{21}}$ to low pass filter the rectified signal and remove 6/Rev. d) Application of anti-aliasing filter

2.2.2. Experimental Results

A comparison of estimated and actual shaft speed and torque for Experiment 1, with fixed axial position, is shown in Figure 2.17. The delay-corrected errors between the two deviate by less than 2.5 RPM and 0.058 ft-lbs (with standard deviations of 0.42 RPM and 0.011 ft-lbs), respectively.

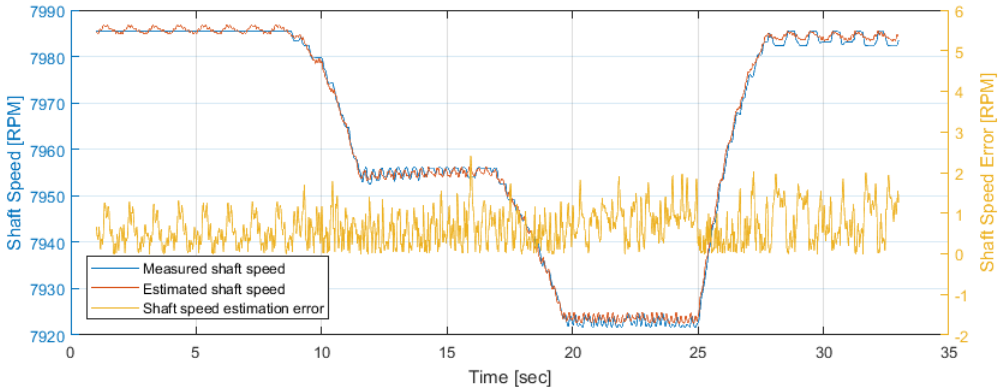

(a)

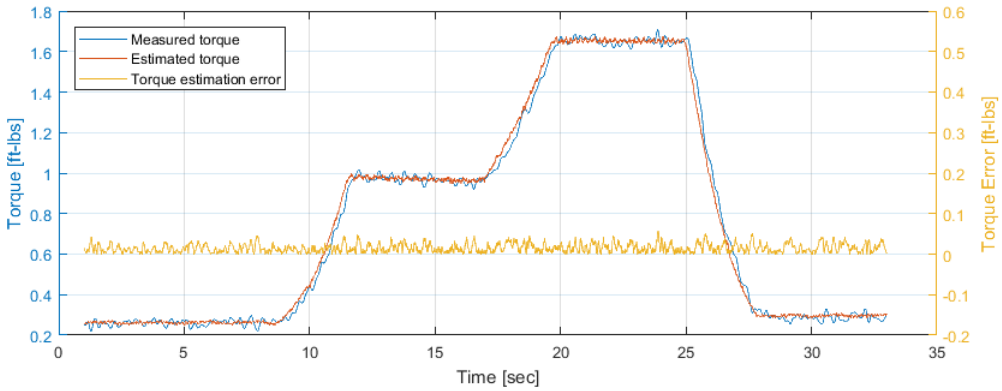

(b)

Figure 2.17: Experiment 1 torque ramp profile showing system performance: a) decreasing shaft speed under additional torsional loading b) actual and torque estimation error

With the application of external torque, shaft speed decreased from the nominal commanded speed of 8,000 RPM (133.3 Hz); this was expected due to the open-loop spindle motor control, thus the motor slipped at higher loads and rotated slightly slower. With the shaft rotating at 8,000 RPM and no external torque applied, a residual torque due to bearing and aerodynamic drag was evident. In addition to measuring the steady-state torque measurements, transient torque profiles were estimated without significant error (less than 4% during Experiment 1).

The estimated profiles for axial position, shaft speed, and torque are presented in Figure 2.18. While there was no reference of comparison for axial position, the delay-corrected error for shaft speed was less than 2.5 RPM (with a standard deviation of 0.42 RPM). Torque estimation error with and without axial calibration remained below 0.37 and 0.15 ft-lbs (with standard deviations of 0.021 and 0.067 ft-lbs), respectively. The estimated axial position (Figure 20a) reveals no evidence of the torque ramp profile, confirming the robustness of the TAP algorithm. Without axial position compensation (Figure 20c), errors in torque estimation were large (21-23% max error); these errors reduce to 6-7% with compensation.

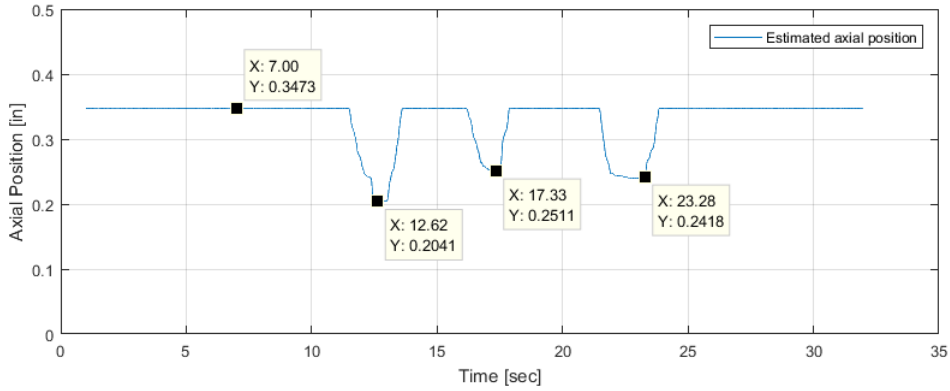

(a)

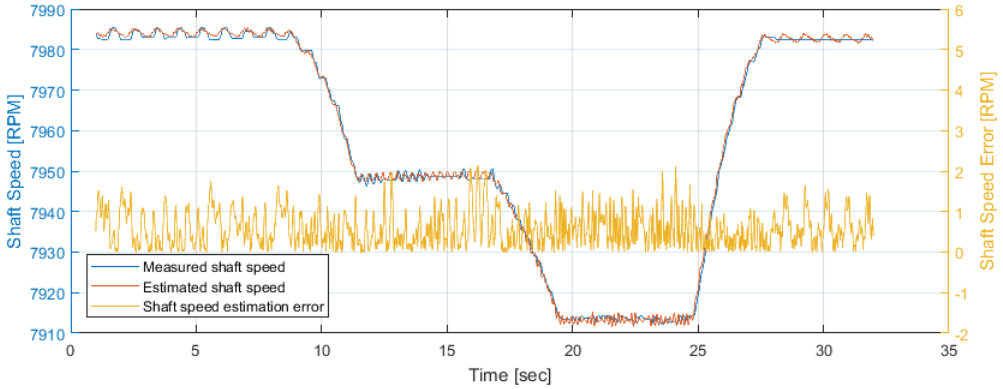

(b)

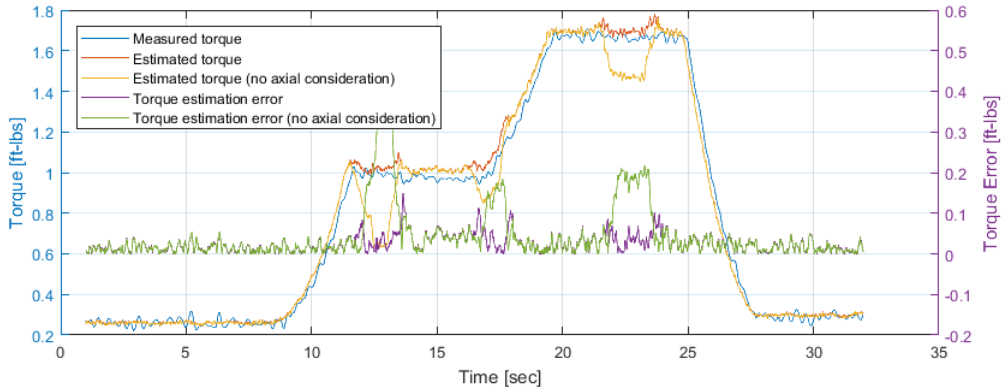

(c)

Figure 2.18: Experiment 2 measured and estimated torque results: a) calibrated axial measurements b) shaft speed profile c) torque profile with and without axial compensation

2.3. Discussion

Simulations and experimental results confirm that the TAP algorithm, which uses data from stationary VR sensors and slanted tooth wheels, accurately estimates speed, torque, and axial translation in high-speed rotating shafts. Simulations reveal accurate estimation of steady-state values and the ability to track low-bandwidth variations in shaft speed, torque, and axial translation, while harmonic torsional motion caused minor estimation errors.

Most driveshaft torque measurement applications involve larger torsional loads (greater than 1000 ft-lbs) than those tested here, resulting in torsional deflections of 1-2 degrees. While the experimental setup detailed here utilized much smaller torsional loads (less than 2 ft-lbs), it used a soft coupling between the toothed wheels, resulting in torsional deflections up to 0.05 degrees. This allowed realistic high-speed estimations of torsional deflections at lower loads. Torque estimation on full-scale setups would likely provide even higher accuracy due to the demonstrated resolution of less than 1 ft-lb.

Experimental results reveal axial translation estimates were accurate over a 0.5-inch range. During axial calibration, the estimated torque varied with axial position, with uncompensated torque estimation errors of 21-23%. With axial position compensation, these torque estimation errors were reduced to 6-7%. The remaining estimation error is difficult to isolate and is possibly due to machining tolerances (causing errors in tooth parallelism) or variations between the cradle’s axial translation and the lab setup’s driveshaft centerline.

Chapter 3: Drivetrain Whirl Estimation

Accurate, real-time measurement of radial misalignment synchronous with the shaft speed (i.e. whirl) is critical to high-speed drivetrains; such information could potentially enable smaller radial engine clearances for enhanced efficiency, feedback for active clearance control (ACC) systems or active magnetic bearings (AMBs), and advanced health monitoring system to detect engine blade failures. Whirl measurement performed on aerospace drivetrains could also enable early warning of potentially catastrophic failures. Mitigating shaft whirl amplitudes could reduce bearing failures and other adverse rotordynamic effects. To address this industry need, a novel shaft whirl estimation (SWE) algorithm that extends the VR sensing and signal processing techniques of Chapter 2, is presented and experimentally validated on a high-speed drivetrain. Production drivetrain VR sensor arrays enable permanent installation, and thus continuous whirl estimation, in harsh aerospace engine environments.

The signal processing algorithms of Chapter 2 enabled real-time estimation of torque, shaft speed, and axial translation [36-37, 65] at bandwidths less than half the shaft speed (<0.5P). Radial motion measurement at bandwidths of <0.5P has also been previously demonstrated using a VR sensor array [36]. In this chapter, the SWE algorithm augments previous signal processing methods by estimating radial whirl at bandwidths synchronous with the shaft speed (1P).

3.1. Methods

VR sensor timing differences are used to accurately estimate twist, torque, axial translation, and radial motion of rotating toothed wheels (e.g. gears) [24]. The SWE system measures shaft whirl (a specific type of radial motion) using six VR sensors mounted into a cradle assembly, which houses the toothed wheels and high-speed rotating shaft (Figure 3.1). The VR cradle secures two arrays of three VR sensors circumferentially spaced at 100° intervals. The shaft has a flexible coupling between the toothed wheels and is driven by a high-speed spindle.

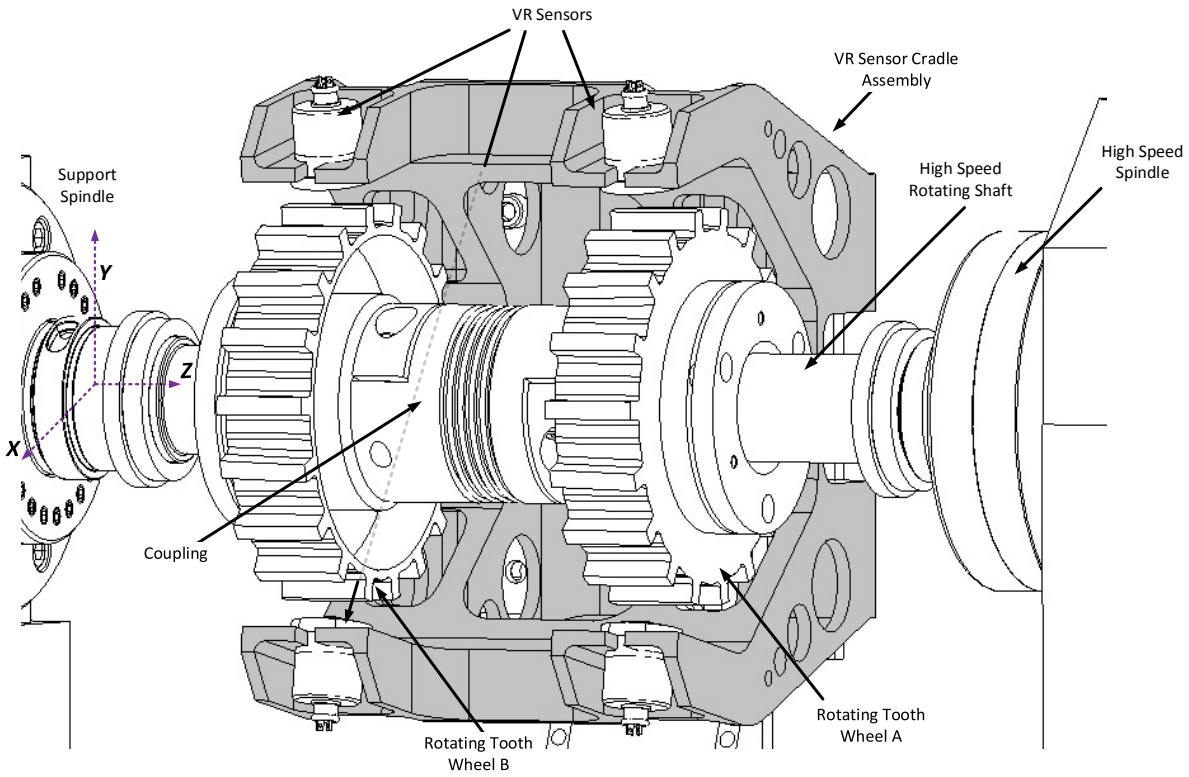

Figure 3.1: Diagram of torque sensing system: cradle with six VR sensors oriented circumferentially around high-speed rotating shaft and flexible coupling with toothed wheels

The rotating toothed wheels *A* and *B* have 18 teeth and are identical to within machining tolerances. Wheel *B* is located on the support spindle side and wheel *A* is located on the high-speed spindle drive side. The three sensors oriented around wheel *A* are designated A_1-A_3 and the sensors oriented around wheel *B* are designated B_1-B_3 (Figure 3.2).

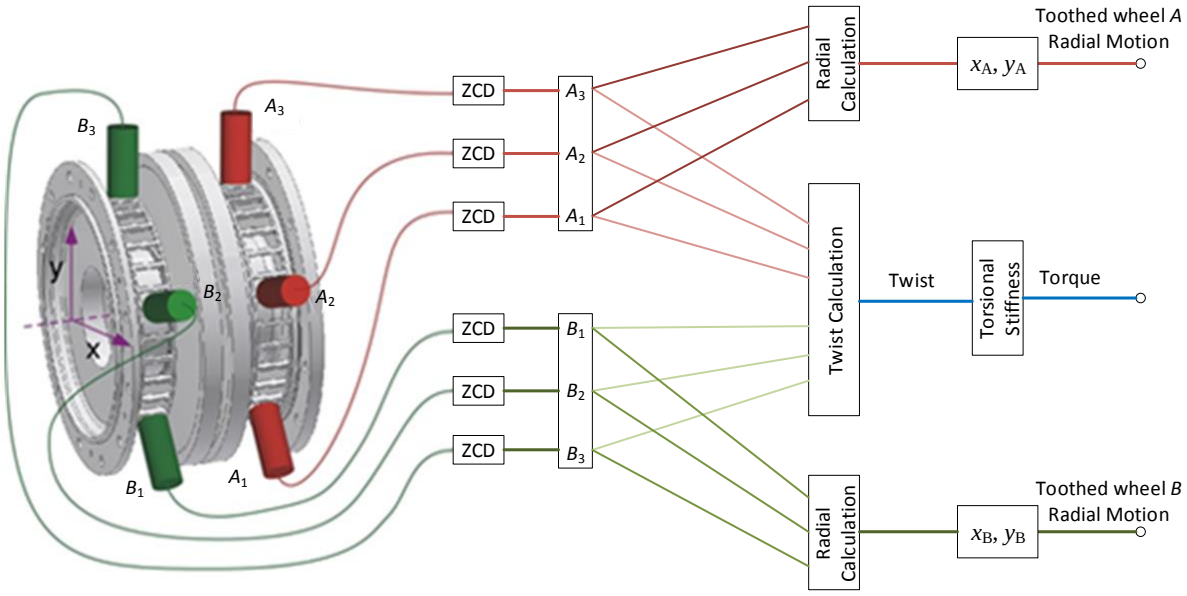

Figure 3.2: Schematic of torque measurement system and processing with VR sensor Zero-Cross Detections (ZCD) and SWE algorithm

As each tooth passes a sensor, a voltage pulse is generated, and a logic signal is produced based on the zero crossings of this voltage (Figure 3.3). On the signal's falling edge, a timing value is acquired at each zero crossing and used in the SWE algorithm processing:

$$\vec{v}^{k} = \left[v_{A_1}^{k} \quad v_{A_2}^{k} \quad v_{A_3}^{k} \quad v_{B_1}^{k} \quad v_{B_2}^{k} \quad v_{B_3}^{k} \right]^{T} \tag{20}$$

where v_i^k indicates the k^{th} zero-crossing time (in microcontroller clock cycles) of the i^{th} sensor.

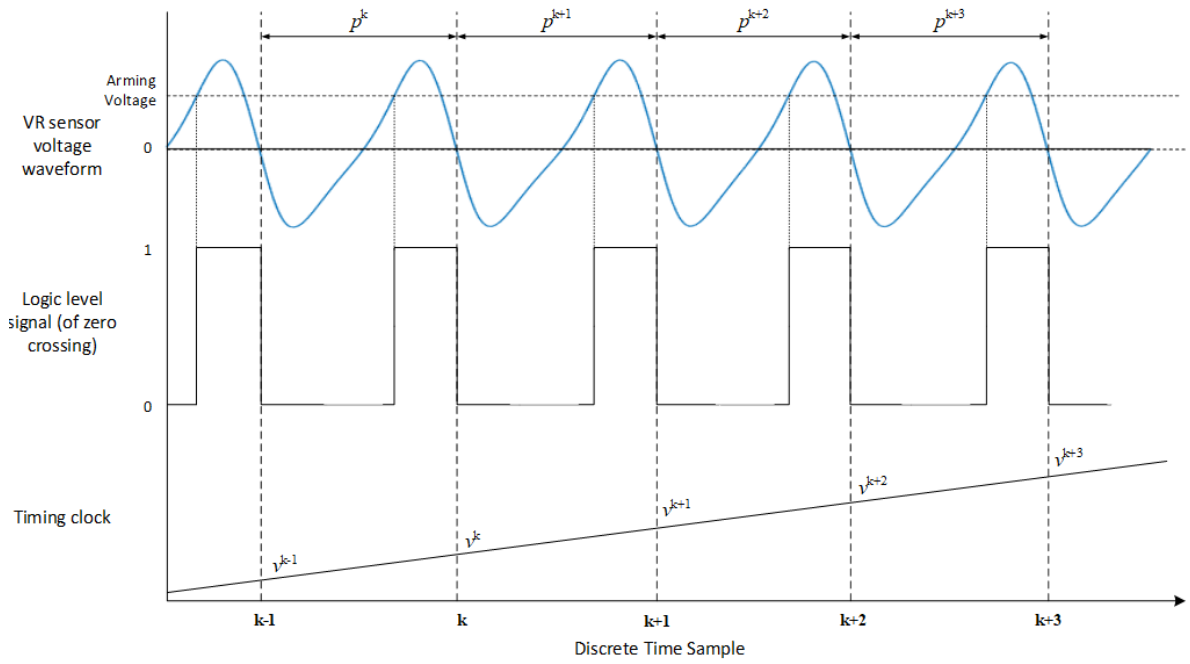

Figure 3.3: VR sensor conditioning schematic: voltage waveform with arming voltage threshold, zero-crossing logic level signal with tooth period $\boldsymbol{p^k}$, and timing clock to capture zero-crossing logic signals

Each sensor's tooth period p_i^k is the time between successive zero crossings:

$$\vec{p}^{\,k} = \begin{bmatrix} p_{A_1}^k \\ p_{A_2}^k \\ p_{A_3}^k \\ p_{B_1}^k \\ p_{B_2}^k \\ p_{B_3}^k \end{bmatrix} = \begin{bmatrix} v_{A_1}^k - v_{A_1}^{k-1} \\ v_{A_2}^k - v_{A_2}^{k-1} \\ v_{A_3}^k - v_{A_3}^{k-1} \\ v_{B_1}^k - v_{B_1}^{k-1} \\ v_{B_2}^k - v_{B_2}^{k-1} \\ v_{B_3}^k - v_{B_3}^{k-1} \end{bmatrix} \tag{21}$$

3.1.1. Signal Processing

The SWE algorithm calculates real-time shaft speed and radial translation based on the zero-crossing time vector $\vec{v}^{k}$. For each VR sensor, *N* successive tooth periods P_i^k are averaged and filtered to quantify the wheel's period P^k (in timing clock cycles) according to the SWE filtering schematic of Figure 3.4.

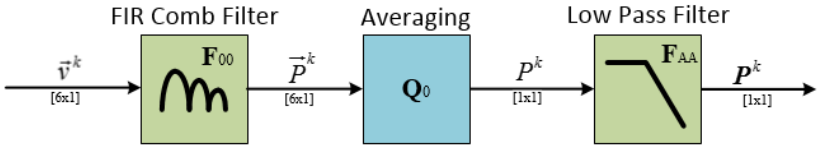

Figure 3.4: SWE filtering schematic to determine clock cycles per revolution

The FIR comb filter $\boldsymbol{F}_{00}$ removes noise and the effects of machining tolerances from the zero-crossings and calculates each sensor's "period of revolution" or P_i^k:

$$P_i^k = p_i^k + p_i^{k-1} + \ldots + p_i^{k-N+2} + p_i^{k-N+1} = \sum_{n=0}^{N-1} p_i^k z^{-n} = \boldsymbol{F}_{00} v_i^k \tag{22}$$

where *N* is the wheel's number of teeth and z^{-n} is the unit delay function. Improved signal-to-noise (SNR) ratio is achieved by averaging across all sensors. A low-pass filter $\boldsymbol{F}_{AA}$, in this case a 2nd-order Butterworth filter, is used to eliminate aliasing in the measurement data, which for typical digital engine controllers is transmitted at rates ranging from 50 to 100 Hz [66].

$$\boldsymbol{P}^k = \boldsymbol{F}_{AA} P^k = \boldsymbol{F}_{AA} \frac{1}{6}\left(\sum_{i=1}^{6} P_i^k \right) = \boldsymbol{F}_{AA} \mathbf{Q}_0 \vec{P}^k \tag{23}$$

The resulting timing clock cycles per revolution ($\boldsymbol{P}^k$) are used to determine shaft speed f_{shaft}^k:

$$f_{\text{shaft}}^k = \frac{f_{\text{clock}}}{\boldsymbol{P}^k} \tag{24}$$

where f_{clock} is the timing clock speed in Hz and f_{shaft}^k is the shaft speed, also in Hz.

While the SWE algorithm calculates radial whirl, radial translation at a bandwidth of <0.5P is illustrated in the filtering schematic (Figure 3.5).

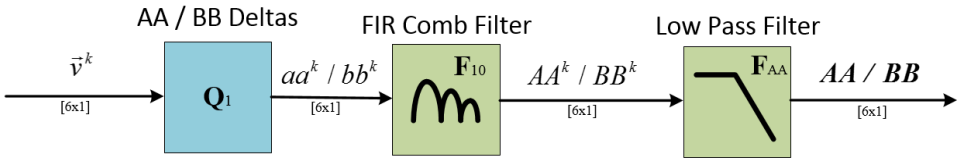

Figure 3.5: Filtering schematic to determine radial translation

The phase differences between each set of three sensors are calculated using matrix math defined by $\boldsymbol{Q}_1$ resulting in a six-element vector $aabb^k$.

$$\overrightarrow{aabb}^k = \begin{bmatrix} v_{A_1}^k - v_{A_2}^k \\ v_{A_2}^k - v_{A_3}^k \\ v_{A_3}^k - v_{A_1}^k \\ v_{B_1}^k - v_{B_2}^k \\ v_{B_2}^k - v_{B_3}^k \\ v_{B_3}^k - v_{B_1}^k \end{bmatrix} = \boldsymbol{Q}_1 \vec{v}^k \tag{25}$$

Typical FIR comb filtering ($\boldsymbol{F}_{10}$) and anti-alias filtering ($\boldsymbol{F}_{AA}$) is applied to these six values to eliminate the effects of machining tolerances and aliasing in the transmitted measurements.

$$\overrightarrow{\boldsymbol{AABB}}^{k} = \boldsymbol{F}_{AA}\boldsymbol{F}_{10}\overrightarrow{aabb}^{k} = \boldsymbol{F}_{AA}\sum_{n=0}^{n=N-1}\frac{z^{-n}\overrightarrow{aabb}^{k}}{N} \tag{26}$$

As before, N is the wheel's number of teeth and z^{-n} is the unit delay function. The $\boldsymbol{AABB}^{k}$ values can be transformed into approximate x and y radial motion using a linear transformation defined in [36] and detailed for a single VR sensor in Figure 3.6.

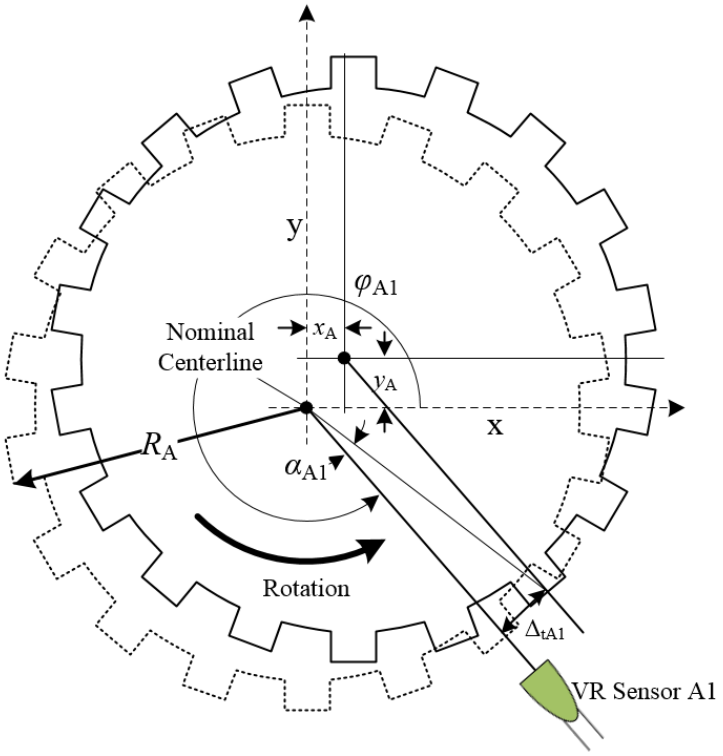

Figure 3.6: Diagram of radial translation and resulting motion at a single VR sensor

Radial motion of the toothed wheel results in tangential motion (Δ_{tA1}) at the VR sensor, which for small radial deflections can be written as the following:

$$\Delta_{tA1} = -x_A \sin(\varphi_{A1}) + y_A \cos(\varphi_{A1}) \tag{27}$$

where φ_{A1} is the angle of the VR sensor about the shaft center of rotation. Tangential motion (Δ_{tA1}) at the VR sensor causes a phase shift in the timing measurement (α_{A1}), which is defined in equation (28):

$$\alpha_{A1} = \frac{\Delta_{tA1}}{R_A} \tag{28}$$

where R_A is the radius of the sensor around the *A* wheel. Extending equation (28) to the other VR sensors and calculating the phase differences between α_{A1} and α_{A2}, α_{A2} and α_{A3}, and α_{A3} and α_{A1}, results in the following relationship between *x* and *y* radial motion and $\boldsymbol{AABB}^k$ values defined in (29).

$$\overrightarrow{\boldsymbol{AABB}}^k = \frac{f_{\text{clock}}}{2\pi f_{\text{shaft}}^k}[\Theta]\begin{bmatrix} x_A / R_A \\ y_A / R_A \\ x_B / R_B \\ y_B / R_B \end{bmatrix} \tag{29}$$

As before, f_{clock} is the timing clock speed in Hz, f_{shaft}^k is the shaft speed in Hz, R_A and R_B are the radii of the *A* and *B* sensors respectively, and the over-determined transformation matrix [Θ] is defined as the following:

$$\left[\Theta\right]=\begin{bmatrix} \sin(\phi_{A2})-\sin(\phi_{A1}) & \cos(\phi_{A1})-\cos(\phi_{A2}) & 0 & 0 \\ \sin(\phi_{A3})-\sin(\phi_{A2}) & \cos(\phi_{A2})-\cos(\phi_{A3}) & 0 & 0 \\ \sin(\phi_{A1})-\sin(\phi_{A3}) & \cos(\phi_{A3})-\cos(\phi_{A1}) & 0 & 0 \\ 0 & 0 & \sin(\phi_{B2})-\sin(\phi_{B1}) & \cos(\phi_{B1})-\cos(\phi_{B2}) \\ 0 & 0 & \sin(\phi_{B3})-\sin(\phi_{B2}) & \cos(\phi_{B2})-\cos(\phi_{B3}) \\ 0 & 0 & \sin(\phi_{B1})-\sin(\phi_{B3}) & \cos(\phi_{B3})-\cos(\phi_{B1}) \end{bmatrix} \quad (30)$$

where φ_{A1}, φ_{A2}, φ_{A3}, φ_{B1}, φ_{B2}, and φ_{B3} are the angles of each sensor with respect to the x axis. Using a pseudo-inverse and the parameters defined in Eqns. (29) and (30), the radial position (x_A, y_A, x_B, and y_B) is determined. The SWE algorithm is an enhancement of the radial motion algorithm to estimate shaft synchronous whirl. This is implemented using the signal processing algorithm of Figure 3.7.

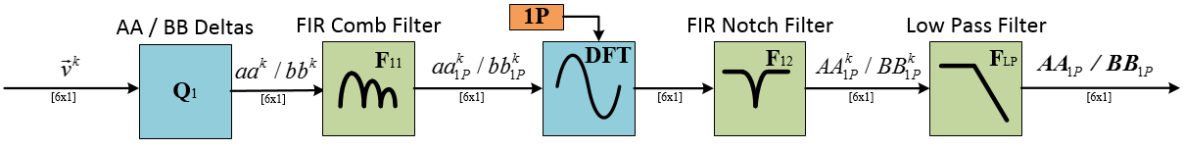

Figure 3.7: Filtering schematic to determine whirl (radial translation at 1P)

The timing differences between *A* and *B* sensors are calculated identically to Eqn. (14) for radial motion. However, the $\boldsymbol{F}_{11}$ filter isolates shaft synchronous content (different than the previously detailed $\boldsymbol{F}_{10}$ filter which eliminates 1P content). $\boldsymbol{F}_{11}$ is a typical FIR filter governed by Eqn. (31) and defined by Table 3.1's coefficients, which can be determined by

taking the $\boldsymbol{F}_{10}$ coefficients and performing a deconvolution of the existing zero at 1P and a convolution of a new zero at DC.

$$\overrightarrow{aabb}^{k}_{1P} = \sum_{n=0}^{n=N-1} B_{11}[n] z^{-n} \overrightarrow{aabb}^{k} \tag{31}$$

Table 3.1: $\boldsymbol{F}_{11}$ filter coefficients

Coefficients	Value
$\boldsymbol{B}_{11}[0]$, $\boldsymbol{B}_{11}[17]$	0.1094
$\boldsymbol{B}_{11}[1]$, $\boldsymbol{B}_{11}[16]$	0.0962
$\boldsymbol{B}_{11}[2]$, $\boldsymbol{B}_{11}[15]$	0.0714
$\boldsymbol{B}_{11}[3]$, $\boldsymbol{B}_{11}[14]$	0.0380
$\boldsymbol{B}_{11}[4]$, $\boldsymbol{B}_{11}[13]$	0.0000
$\boldsymbol{B}_{11}[5]$, $\boldsymbol{B}_{11}[12]$	-0.0380
$\boldsymbol{B}_{11}[6]$, $\boldsymbol{B}_{11}[11]$	-0.0714
$\boldsymbol{B}_{11}[7]$, $\boldsymbol{B}_{11}[10]$	-0.0962
$\boldsymbol{B}_{11}[8]$, $\boldsymbol{B}_{11}[9]$	-0.1094

Figure 3.8 compares the Bode diagrams and root locus plots of both the $\boldsymbol{F}_{10}$ and $\boldsymbol{F}_{11}$ filter.

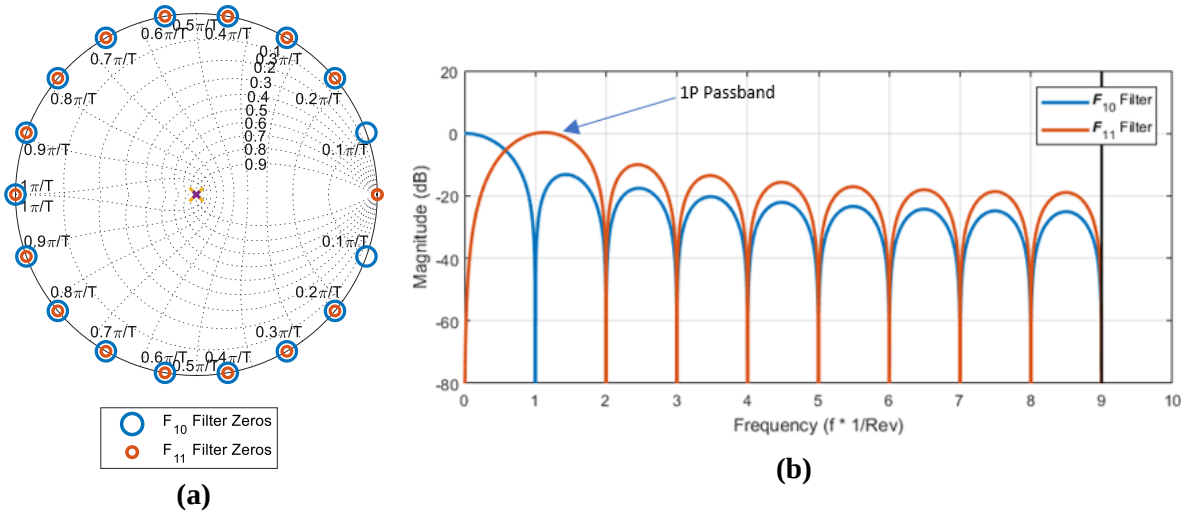

Figure 3.8: $\boldsymbol{F_{10}}$ and $\boldsymbol{F_{11}}$ filter characteristics. a) Root locus plots showing filter zeros and origin poles along a grid of constant damping, where large circles and small circles indicate $\boldsymbol{F_{10}}$ and $\boldsymbol{F_{11}}$ filter zeros, respectively. b) Bode plot of filters indicating passband at 1P for $\boldsymbol{F_{11}}$ filter

The notch that previously existed in the $\boldsymbol{F}_{10}$ filter is removed (allowing 1P content to pass), and DC content is removed. This filter isolates the 1P radial shaft motion, as desired, though machining tolerances could result in 1P timing content that is not a result of shaft whirl effects, resulting in shaft whirl estimation errors.

With the 1P content isolated, quadrature amplitude demodulation techniques can be applied to assess the 1P magnitude and phase [67]. Signal demodulation by a complex exponent results in the following relationship:

$$\overrightarrow{aabb}^{k}_{1P,DFT} = 2e^{-j\theta_{1P}}\overrightarrow{aabb}^{k}_{1P} = \boldsymbol{DFT}_{1P}\boldsymbol{F}_{11}\overrightarrow{aabb}^{k} \tag{32}$$

where θ_{1P} is the 1P shaft angle, and j is the complex square root of –1. After the demodulation, frequency content is contained at two major frequencies: DC and 2P, as expected [68]. Because the 2P content is not desirable, a FIR notch filter $\boldsymbol{F}_{12}$ is applied to remove the 2P content. The filter coefficients and mathematical application are defined in Table 3.2 and Eqn. (34).

$$\overrightarrow{AABB}_{1P}^{k} = \boldsymbol{F}_{12}\boldsymbol{DFT}_{1P}\boldsymbol{F}_{11}\overrightarrow{aabb}^{k} \tag{33}$$

Table 3.2: $\boldsymbol{F}_{12}$ filter coefficients

Coefficients	Value
$\boldsymbol{B}_{12}[0]$	2.1372
$\boldsymbol{B}_{12}[1]$	-3.2743
$\boldsymbol{B}_{12}[2]$	2.1372

$$\overrightarrow{AABB}_{1P}^{k} = \sum_{n=0}^{n=N-1} B_{12}[n]z^{-n}\overrightarrow{aabb}_{1P,DFT}^{k} \tag{34}$$

A low pass, anti-alias filtering $\boldsymbol{F}_{LP}$ is applied to the signal to limit the demodulation bandwidth and allow for appropriate decimation to a lower speed of calculation (80 – 100 Hz).

$$\overrightarrow{\boldsymbol{AABB}}_{1P}^{k} = \boldsymbol{F}_{LP}\overrightarrow{AABB}_{1P}^{k} = \boldsymbol{F}_{LP}\boldsymbol{F}_{12}\boldsymbol{DFT}_{1P}\boldsymbol{F}_{11}\overrightarrow{aabb}^{k} \tag{35}$$

The six-element $\boldsymbol{AABB}_{1P}$ vector can be converted with the same matrix system in Eqn. (30) to estimate x and y whirl motion of each toothed wheel.

$$\overrightarrow{\boldsymbol{AABB}}_{1P}^{k} = \frac{f_{\text{clock}}}{2\pi f_{\text{shaft}}^{k}}\left[\Theta\right]\begin{bmatrix} x_{A,1P}/R_A \\ y_{A,1P}/R_A \\ x_{B,1P}/R_B \\ y_{B,1P}/R_B \end{bmatrix} \tag{36}$$

Once the demodulated radial positions ($x_{A,1P}$, $y_{A,1P}$, $x_{B,1P}$, and $y_{B,1P}$) are known, they can be manipulated into orbital plots helpful for visualizing whirl. Since these demodulated positions are complex, Eqn. (37) is used to determine (X_A, Y_A) coordinates for each plotted rotor orbit point of the *A* wheel:

$$\begin{bmatrix} X_A \\ Y_A \end{bmatrix} = \begin{bmatrix} \text{Re}[x_{A,1P}] & \text{Im}[x_{A,1P}] \\ \text{Re}[y_{A,1P}] & \text{Im}[y_{A,1P}] \end{bmatrix}\begin{bmatrix} \cos(\theta) \\ \sin(\theta) \end{bmatrix} \tag{37}$$

where θ is a vector of angles from 0 to 2π that allows an enclosed orbit to be calculated.

3.1.2. Computer Simulations

The SWE algorithm performance in estimating shaft speed and radial translation can be evaluated via numerical computer simulations, like previous evaluations of shaft torque and axial translation [65]. Phase shifts in the VR timing measurement can be related to shaft motion and sensor geometrical properties (R: radius of sensors and φ_i: angle of the i^{th} sensor) using Eqn. (38) [36]:

$$\alpha_i = \varphi_i - \tan^{-1}\left(\frac{R\sin\varphi_i - y_i}{R\cos\varphi_i - x_i}\right) \tag{38}$$

where x_i and y_i are the radial translation associated with the i^{th} sensor. By applying Eqn. (38) to each sensor, zero-crossing timing vectors $\vec{v}^k$ can be simulated for a variety of shaft speeds f_{shaft}^k and radial displacements of each wheel:

$$\vec{v}^k = \frac{f_{clock}}{N}\int_{k'=0}^{k'=k}\frac{dk'}{f_{\text{shaft}}^{k'}} + \frac{f_{\text{clock}}}{f_{\text{shaft}}^k}\begin{bmatrix} \varphi_{A1} - \tan^{-1}\left(\dfrac{R_A\sin\varphi_{A1} - y_A^k}{R_A\cos\varphi_{A1} - x_A^k}\right) \\ \varphi_{A2} - \tan^{-1}\left(\dfrac{R_A\sin\varphi_{A2} - y_A^k}{R_A\cos\varphi_{A2} - x_A^k}\right) \\ \varphi_{A3} - \tan^{-1}\left(\dfrac{R_A\sin\varphi_{A3} - y_A^k}{R_A\cos\varphi_{A3} - x_A^k}\right) \\ \varphi_{B1} - \tan^{-1}\left(\dfrac{R_B\sin\varphi_{B1} - y_B^k}{R_B\cos\varphi_{B1} - x_B^k}\right) \\ \varphi_{B2} - \tan^{-1}\left(\dfrac{R_B\sin\varphi_{B2} - y_B^k}{R_B\cos\varphi_{B2} - x_B^k}\right) \\ \varphi_{B3} - \tan^{-1}\left(\dfrac{R_B\sin\varphi_{B3} - y_B^k}{R_B\cos\varphi_{B3} - x_B^k}\right) \end{bmatrix} \tag{39}$$

where x_A, y_A, x_B, and y_B are the radial translations associated with each toothed wheel, φ_{A1}, φ_{A2}, φ_{A3}, φ_{B1}, φ_{B2}, and φ_{B3} are sensor angles, R_A is the A wheel sensor radius, R_B is the B wheel sensor radius, and N is the number of teeth. Since the phase shift α_i is non-linearly related in Eqn. (38) to x and y translation, and the SWE algorithm approximated the phase shift linearly in Eqn. (29), some radial estimation error is expected as shown in Figure 3.9.

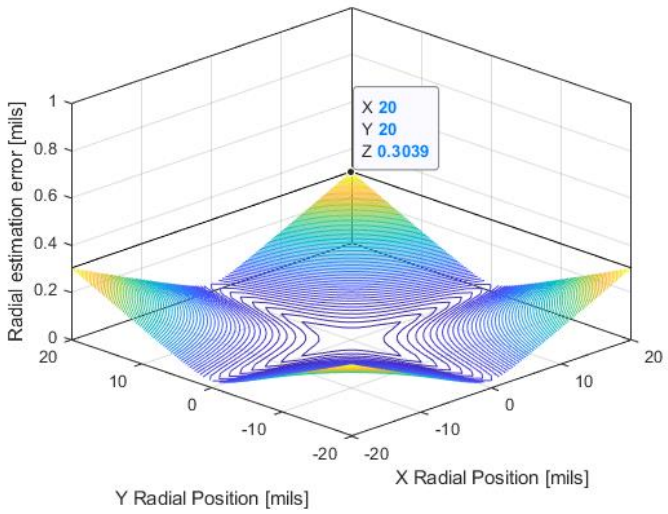

Figure 3.9: Simulation of radial estimation error based on SWE algorithm's linear approximation of VR sensor phase shifts

While the estimation errors never exceeded 0.304 mils (at values of *x* and *y* which are greater than simulation values and experimental testing), more significant errors resulted with a combination of simultaneous *x* and *y* translation. Results shown in Figure 3.9 indicated that the linear approximation in the SWE algorithm is justified for the expected *x* and *y* translations, and do not contribute significantly to SWE measurement errors.

Using MATLAB 2018b, timing vectors were simulated over 30 seconds for two cases: 1. Increasing shaft whirl at a constant shaft speed; 2. Increasing shaft whirl as shaft speed increases. Table 3.3 summarizes the simulation parameters used for both cases.

Table 3.3: Simulation parameters and geometric constants

Parameter	Variable	Value
Radius of *A* toothed wheel	R_A	2.179 [in]
Radius of *B* toothed wheel	R_B	2.179 [in]
Number of teeth	N	18
Clock speed of measurement	f_{clock}	200 [MHz]
Angle of VR sensors A_1 and B_1	φ_{A1}, φ_{B1}	-100 [°]
Angle of VR sensors A_2 and B_2	φ_{A2}, φ_{B2}	0 [°]
Angle of VR sensors A_3 and B_3	φ_{A3}, φ_{B3}	100 [°]
Anti-aliasing filter ($\boldsymbol{F}_{AA}$) order	n	2
Anti-aliasing filter ($\boldsymbol{F}_{AA}$) cutoff	f_b	133.3 [Hz]
Demodulation low-pass filter ($\boldsymbol{F}_{LP}$) order	N	2
Demodulation low-pass filter ($\boldsymbol{F}_{LP}$) cutoff	f_b	10 [Hz]
x axis radial offset of *B* toothed wheel	x_b	0 [in]
y axis radial offset of *B* toothed wheel	y_b	0 [in]

3.1.2.1.Simulation 1: Constant shaft speed, increasing shaft whirl

Typical operation of a VR drivetrain monitoring system with the SWE algorithm implemented was considered in Simulation 1: a shaft rotating at a constant speed, but with whirl increasing. These events occur during events where a driveshaft balancing weight or compressor blade becomes detached from the high-speed shaft, resulting in self-excited shaft unbalance whirl. Table 3.4 details the simulation profiles where the radial offsets occur at the shaft frequency.

Table 3.4: Shaft speed and radial offsets used in Simulation 1

Time [sec]	Shaft Speed [RPM]	f_{shaft}	Radial offset of *A* toothed wheel CG [mils]	x_A, y_A
$0.0 \leq t \leq 7.5$	5000		$1 \exp(j\, 2\pi\, f_{shaft}\, t)$	
$7.5 < t \leq 10.0$			$(1.6t - 11) \exp(j\, 2\pi\, f_{shaft}\, t)$	
$10.0 < t \leq 15.0$			$5 \exp(j\, 2\pi\, f_{shaft}\, t)$	
$15.0 < t \leq 17.5$			$(-25 + 2t) \exp(j\, 2\pi\, f_{shaft}\, t)$	
$17.5 < t \leq 22.5$			$10 \exp(j\, 2\pi\, f_{shaft}\, t)$	
$22.5 < t \leq 25.0$			$(55 - 2t) \exp(j\, 2\pi\, f_{shaft}\, t)$	
$25.0 < t \leq 30.0$			$5 \exp(j\, 2\pi\, f_{shaft}\, t)$	

3.1.2.2.Simulation 2: Increasing shaft speed and shaft whirl

The second SWE algorithm simulation considered increasing shaft speed and whirl, which occurs during speed transients where the force generated by shaft imbalances increases with speed. Assuming the operating speed remains significantly below the shaft's first critical speed, whirl increases proportionally with shaft speed squared [51, 69]. Table 3.5 details the simulation profiles where the radial offsets occur at the changing shaft frequency.

Table 3.5: Shaft speed and radial offsets used in Simulation 2

Time [sec]	Shaft Speed [RPM]	f_{shaft}	Radial offset of *A* toothed wheel CG [mils]	x_A, y_A
$0.0 \leq t \leq 7.5$	5000		$\exp(j\, 2\pi \int f_{shaft}\, dt)$	
$7.5 < t \leq 10.0$	$5000 + 400\,(t - 7.5)$		$(1 + (t - 7.5)^2/6.25) \exp(j\, 2\pi \int f_{shaft}\, dt)$	
$10.0 < t \leq 15.0$	6000		$2 \exp(j\, 2\pi \int f_{shaft}\, dt)$	
$15.0 < t \leq 17.5$	$6000 + 400\,(t - 15)$		$(1 + (t - 12.5)^2/6.25) \exp(j\, 2\pi \int f_{shaft}\, dt)$	
$17.5 < t \leq 22.5$	7000		$5 \exp(j\, 2\pi \int f_{shaft}\, dt)$	
$22.5 < t \leq 25.0$	$7000 - 800\,(t - 22.5)$		$(1 + 4(t - 25)^2/6.25) \exp(j\, 2\pi \int f_{shaft}\, dt)$	
$25.0 < t \leq 30.0$	5000		$\exp(j\, 2\pi \int f_{shaft}\, dt)$	

3.1.3. Experimental Testing

To experimentally validate a VR drivetrain health monitoring system, especially the SWE algorithm's shaft speed and whirl monitoring capabilities, a laboratory test rig capable of rotating the shaft and toothed wheels at high speeds was constructed (Figure 3.10). This test rig consisted of a high-speed machine tool spindle (Fischer MFM-1224/24, Racine, WI) driving a 30mm diameter steel shaft with a flexible coupling (R&W America, BK2-30-69, Bensenville, IL) between two toothed wheels. An electromagnetic (eddy-current) brake (Magtrol BHB-6B, Buffalo, NY) was used to apply torque, which was measured using a reference transducer (Magtrol TM 307/011, Buffalo, NY). Two magnetic encoders (Lika SMRI5-L-1-32-N-L10-J, Columbus, OH) and their corresponding magnetic rings (Lika MRI/48C-32-5-35, Columbus, OH) were incorporated to measure reference twist.

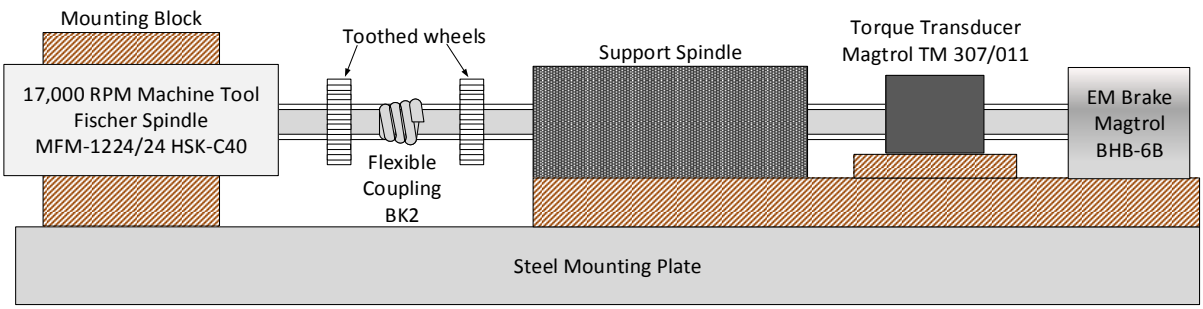

(a)

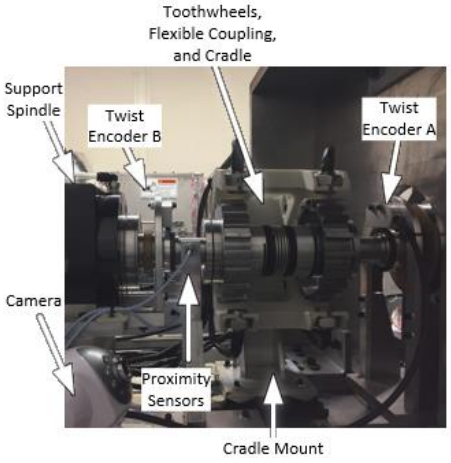

(b)

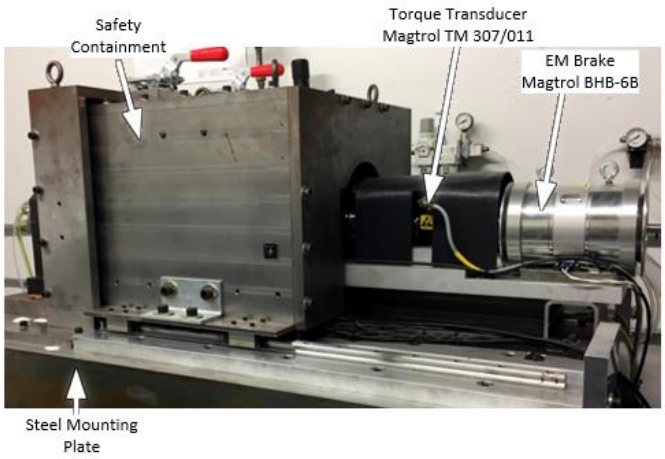

(c)

Figure 3.10: Experimental test rig: a) Block diagram of experimental test rig b) Photograph of the left portion of the test rig showing high speed spindle, toothed wheels, cradle, coupling, and support spindle c) Photograph of the right portion showing the support spindle, the torque transducer, electromagnetic brake, and steel mounting plate

This test rig enabled testing at realistic rotational speeds of up to 15,000 RPM. The flexible coupling was sized to ensure that the spindle torque produced no measurable twist, but allowed slight radial misalignments between the 30mm driveshafts. The cradle and its associated mounting brackets were attached to a two-axis micrometer slide, which allowed axial translation and horizontal radial translation to be simulated by moving the cradle in the *x* and *z* direction. This allowed precise displacements as small as 1 mil that could be

correlated to sensor measurements. All high-speed, high-energy drivetrain components were contained in within a ¾" steel enclosure for safety, as parts rotating at these speeds posed a significant safety risk if mechanical failure occurred.

The six VR sensor outputs were transmitted via shielded cables to customized signal processing hardware (Figure 3.11).

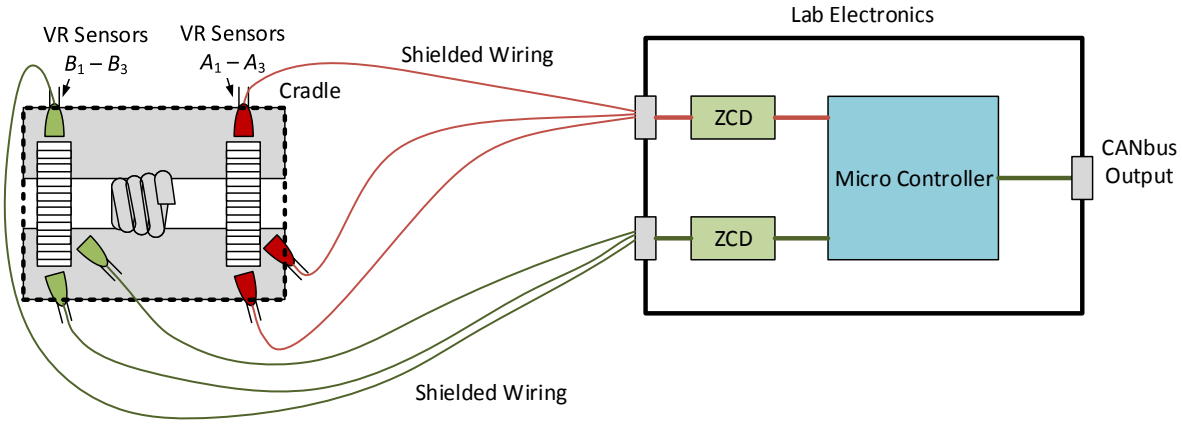

Figure 3.11: Schematic of sensor wiring to processing electronics

VR sensor zero-crossing detection (ZCD) was implemented using an integrated circuit designed specifically for this purpose. The resulting digital signal was routed to a dual-core 200 MHz microcontroller (Texas Instruments LAUNCHXL-F28379D) for real-time filtering and calculation. SWE algorithm results were output to a CANbus for data recording purposes.

3.1.3.1.Experimental calibration

Preliminary testing was conducted to calibrate the experimental setup and SWE algorithm. The toothed wheels were precisely aligned with the cradle sensors, and feeler

gauges were used to measure a gap of roughly 0.190” between sensors and teeth (Figure 3.12); this required setting the horizontal slide position of the two-axis slide’s x-axis to 200 mils. Speed and <0.5P bandwidth radial position (x_A, y_A, x_B, and y_B) were recorded via CANbus at an 83 Hz sample rate; 1P whirl motion variables ($x_{A,1P}$, $y_{A,1P}$, $x_{B,1P}$, and $y_{B,1P}$) were recorded at 125 Hz. Table 3.6 summarizes the experimental parameters used to implement the SWE algorithm.

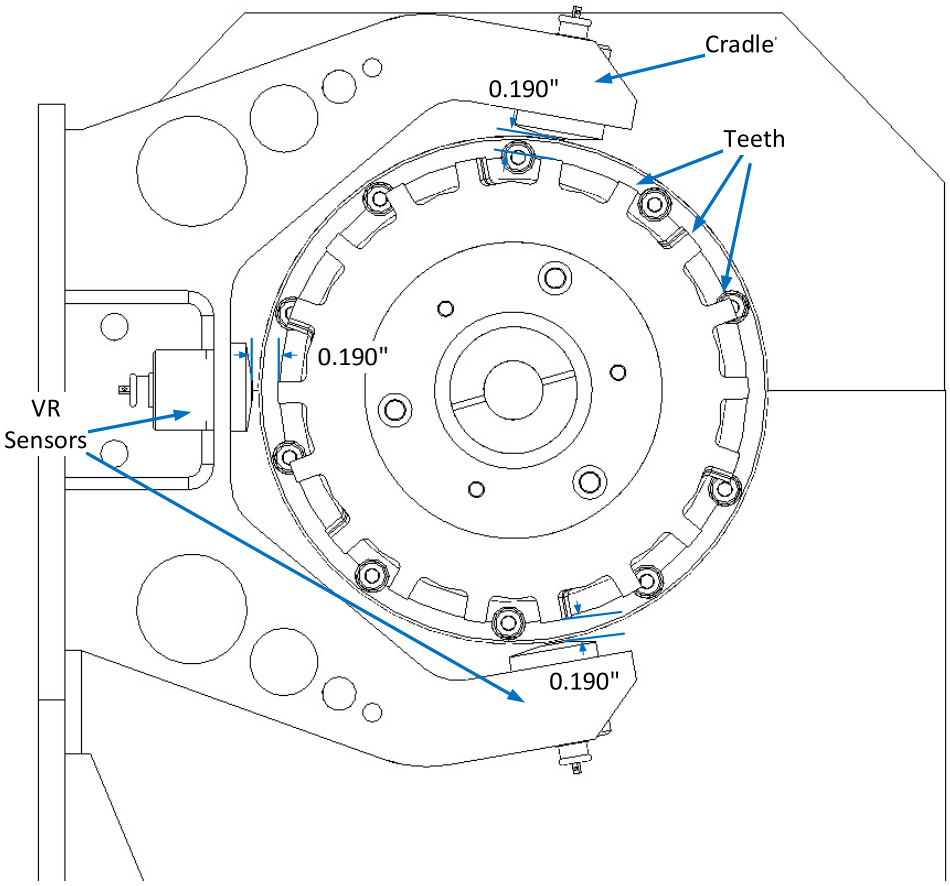

Figure 3.12: Schematic of centered cradle and toothed wheels

Table 3.6: Experimental parameters

Parameter	Variable	Value
Radius of *A* side cradle sensors	R_A	2.4782[in]
Radius of *B* side cradle sensors	R_B	2.5012[in]
Number of teeth	N	18
Clock speed of measurement	f_{clock}	200 [MHz]
Axial slide position	z	250 [mils]
Radial Slide Position	x	200 [mils]
Anti-aliasing filter ($\boldsymbol{F}_{AA}$) order	n	2
Anti-aliasing filter ($\boldsymbol{F}_{AA}$) cutoff	f_b	15 [Hz]
Demodulation low-pass filter ($\boldsymbol{F}_{LP}$) order	n	2
Demodulation low-pass filter ($\boldsymbol{F}_{LP}$) cutoff	f_b	10 [Hz]

Radial position calibration was performed by adjusting the two-axis slide's micrometer dial while the shaft was stopped, and then rotating up to 5,000 RPM. This process was repeated while the dial was adjusted in 50 mil increments from 100 mils to 350 mils, which resulted in 6 discrete measurements. The radial position estimates from calibration testing are presented in Figure 3.13.

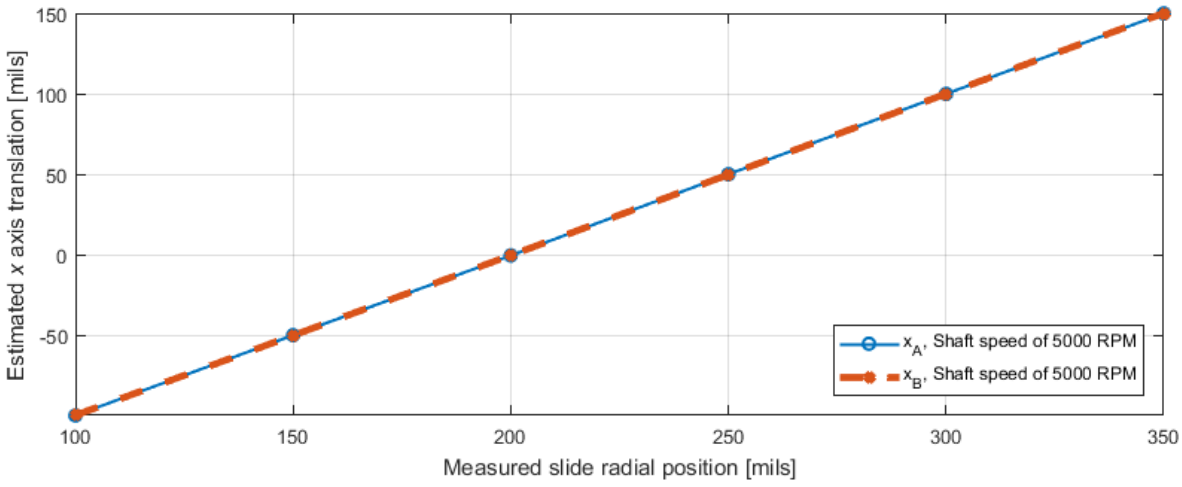

Figure 3.13: Calibrated radial estimates of x_A and x_B from preliminary testing showing linear trend with radial slide position

Throughout the 250 mil measurement range, the estimated radial position remains accurate with errors on the *A* and *B* side below 1 mil at a shaft speed of 5,000 RPM. This error did not fluctuate with shaft speed as significant estimation errors did not occur until operation below 1,000 RPM.

3.1.3.2.Experiment 1: Constant speed, variable whirl

To assess shaft whirl measurement capability, the SWE algorithm was implemented on the test stand limited to a shaft speed of 5,000 RPM. To change the whirl, or orbiting, of the drivetrain, collets were manufactured with nominal offsets of 5 mils and 10 mils (Figure 3.14a) and integrated into the test stand drivetrain (Figure 3.14b).

Integrating precision machined offsets allowed a confirmed measurement of whirl magnitude to verify the SWE algorithm estimated whirl. Precision measurements of the collets' offset (using CMM concentricity measurements) and the overall runout when installed on the test drivetrain are summarized in Table 3.7; at relatively low shaft speeds, static measurements provide a close approximation of shaft whirl. Test data was recorded at a steady state shaft speeds from 2,500 RPM to 5,000 RPM with each collet installed resulting in three distinct test conditions.

Table 3.7: Precision collet measurement summary at static conditions

Collet Description	**Nominal offset of collet [mils]**	**Measured offset of collet [mils]**	**Projected runout on collet installed on drivetrain [mils]**
No offset	0	0.5	0.5
5 mil offset	5	5.5	6.0
10 mil offset	10	10.1	10.6

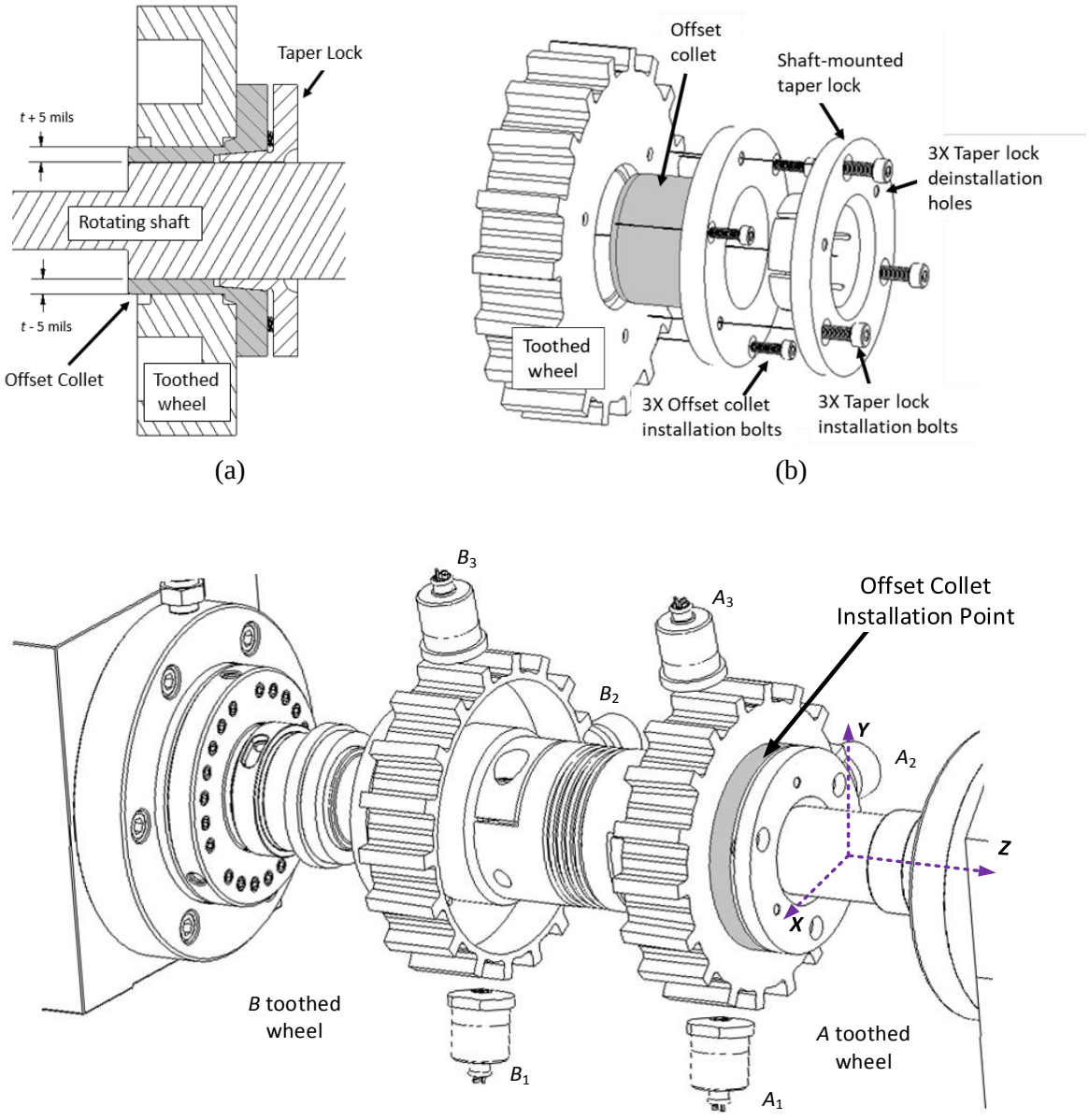

Figure 3.14: Offset collet design and test stand implementation: a) cross-section view showing taper lock and offset collet around shaft and b) exploded view of tooth wheel, offset collet, and taper lock assembly. c) integration point on test stand to create controllable shaft whirl on *A* toothed wheel

3.1.3.3.Experiment 2: Variable speed and whirl

SWE algorithm performance over shaft speed variations was tested using a toothed wheel (with a nominal, no-offset collet) operating at high shaft speeds. The drivetrain shaft speed varied from 3,000 to 12,000 RPM over 50 seconds – simulating a drivetrain transient.

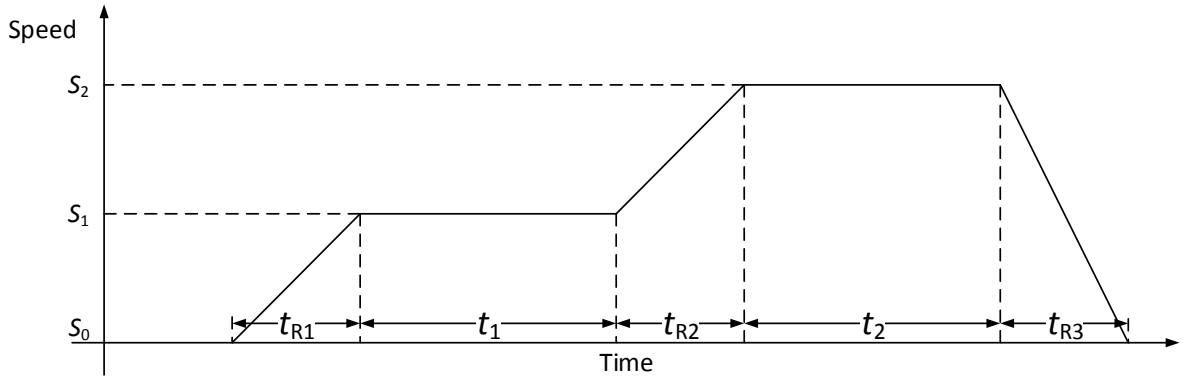

Figure 3.15: Experiment 2 variable speed profile

Table 3.8: Ramp profile parameters for Experiment 2

Parameter	Symbol	Value
First ramp time	t_{R1}	7 [sec]
Second ramp time	t_{R2}	4.5 [sec]
Third ramp time	t_{R3}	11.5 [sec]
Dwell time at S_1	t_1	7 [sec]
Dwell time at S_2	t_2	8 [sec]
Initial speed	S_0	3000 [RPM]
Second speed	S_1	8000 [RPM]
Third speed	S_2	12000 [RPM]

These speeds were deemed safe as resonance assessment profile (RAP) testing on the drivetrain indicated that the pitching modes of each shaft would occur around 12,000 RPM and 19,000 RPM as indicated by the system modal response (Figure 3.16). A DyRoBes rotor analysis predicted the first shaft lateral bending (or critical) mode at 25,000 RPM.

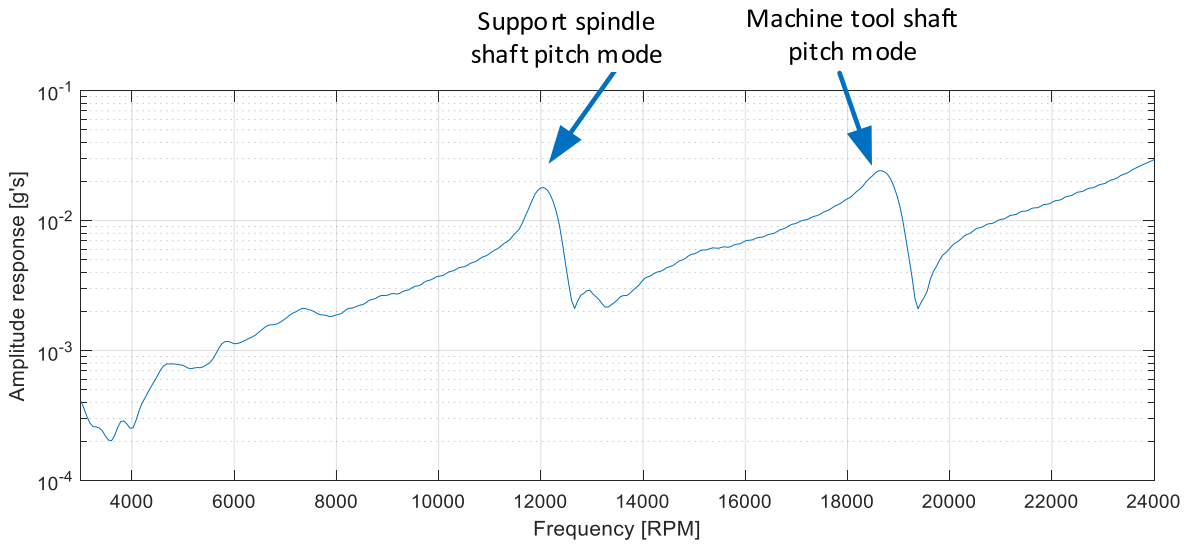

Figure 3.16: Modal response of test stand drivetrain measured with shaft mounted accelerometer showing first two rigid body shaft modes

Measured runout (at static conditions) on the installed toothed wheel and collet assembly was approximately 0.5 mils. Thus, any increase from this level resulted from self-excited shaft unbalance whirl. Throughout the test condition, whirl was continuously estimated during speed transients.

3.2. Results

3.2.1. Simulation Results

Assessing the SWE algorithm performance at steady state shaft speeds was performed in Simulation 1. A comparison of the estimated and actual shaft speed and 1P radial whirl is shown in Figure 3.17. The delay-corrected errors deviated less than 0.002 RPM and 0.03 mils, where most error occurs during the start and end of transient conditions. As the whirl

motion increased (corresponding to a physical event of the rotor imbalance increasing), the estimated x_A and y_A motion increased to an error under one ten-thousandth of an inch (visible in Figure 3.17c) and originate from the $\boldsymbol{F}_{LP}$ IIR filter's response time.

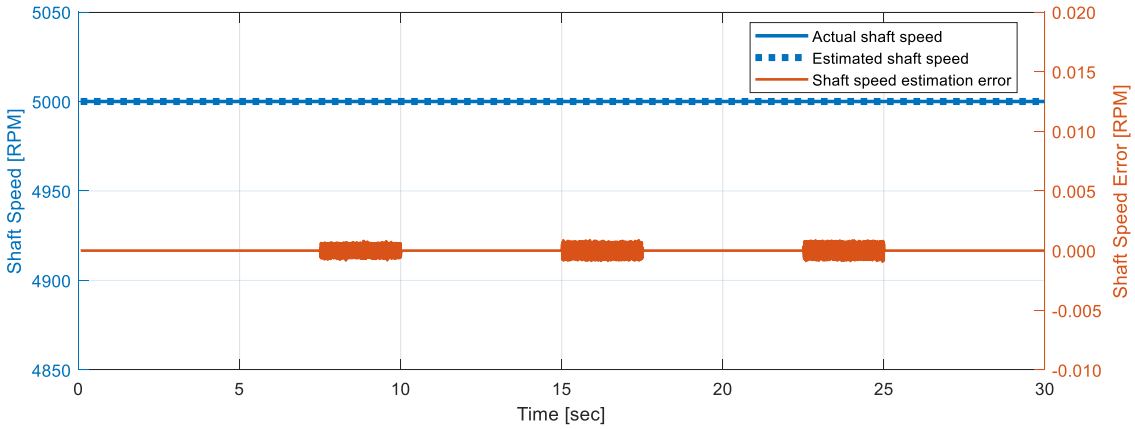

(a)

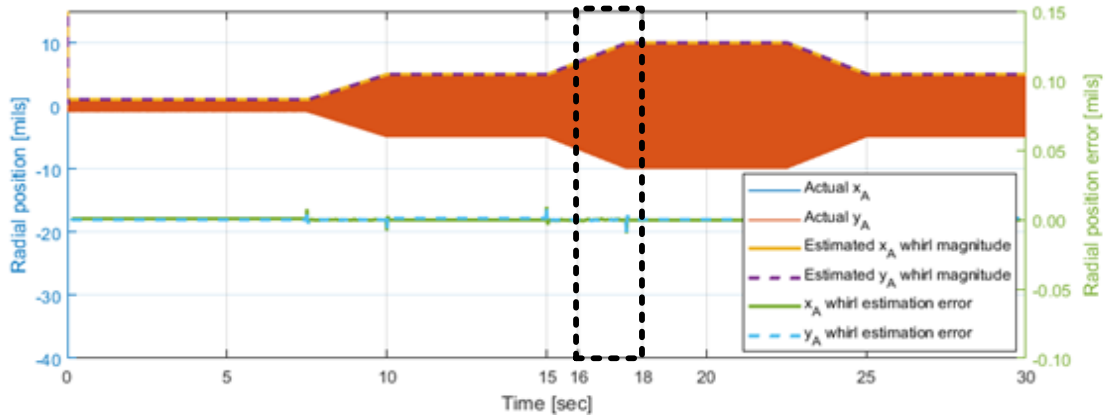

(b)

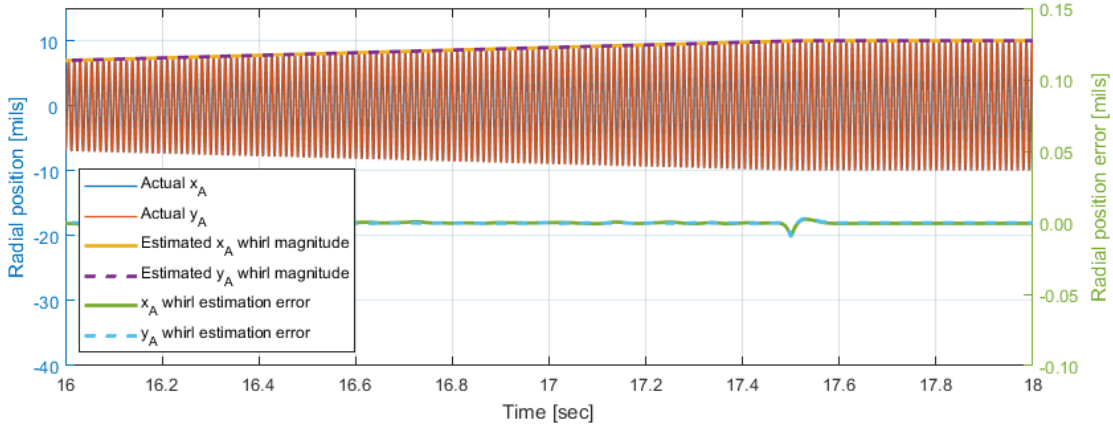

(c)

Figure 3.17: Simulation 1 results for a fixed shaft speed of 5,000 RPM: (a) estimated and actual shaft speed and error; (b) estimated and actual 1P radial whirl and error over entire simulation; (c) whirl and error over 16 to 18 seconds during whirl transient.

While Simulation 1 had a steady shaft speed, Simulation 2 had a variable shaft speed through transient conditions allowing investigation of the SWE algorithm's ability to estimate transient whirl. A comparison of estimated and actual shaft speed and radial whirl for Simulation 2, where both shaft speed and whirl were changing, is presented in Figure 3.18. SWE-estimated shaft speed and 1P radial whirl are indistinguishable from the actual (simulated) profiles, with estimation errors below 5 RPM and 0.03 mils, respectively. Although the shaft speed (and thus the 1P whirl frequency) changes, the SWE whirl estimation remained accurate throughout the simulation, with some additional error observed during the transient conditions where whirl increased as a function of speed squared. The sinusoidal whirl's decreasing frequency and negligible signal unsteadiness can be observed in Figure 3.18c.

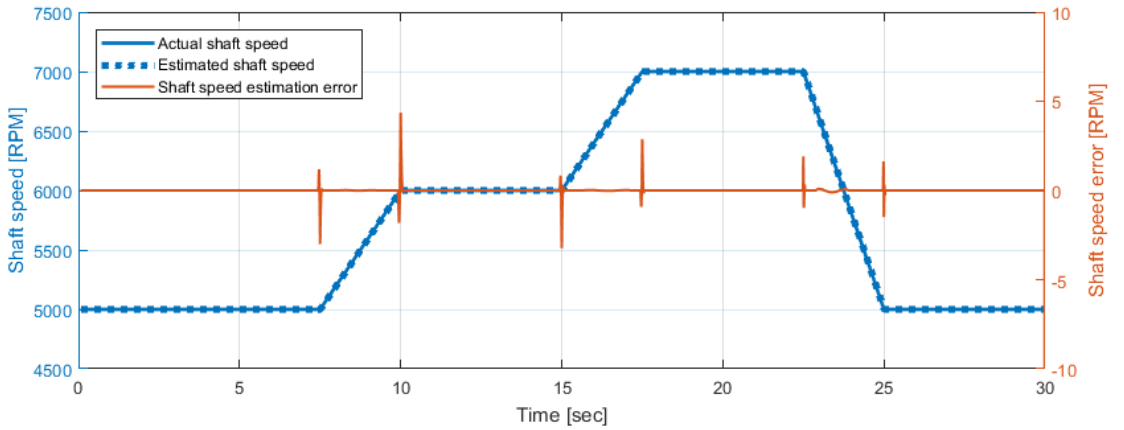

(a)

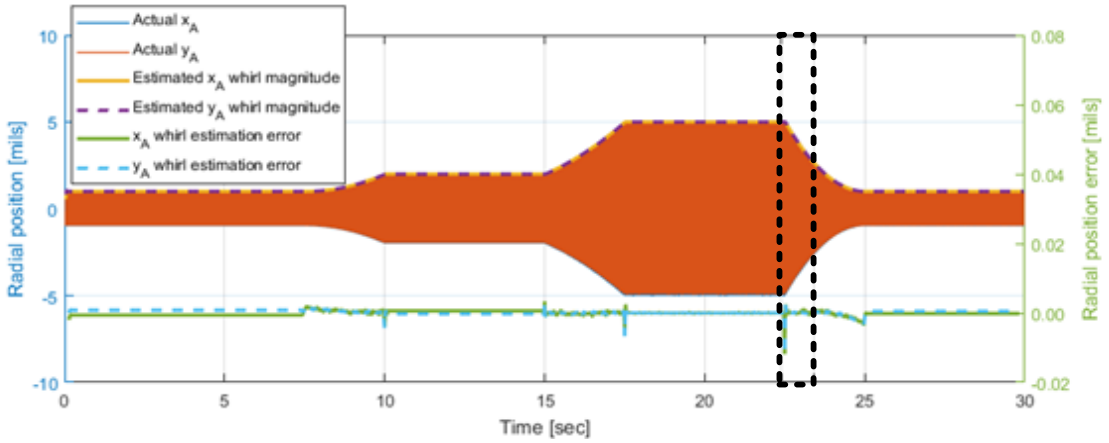

(b)

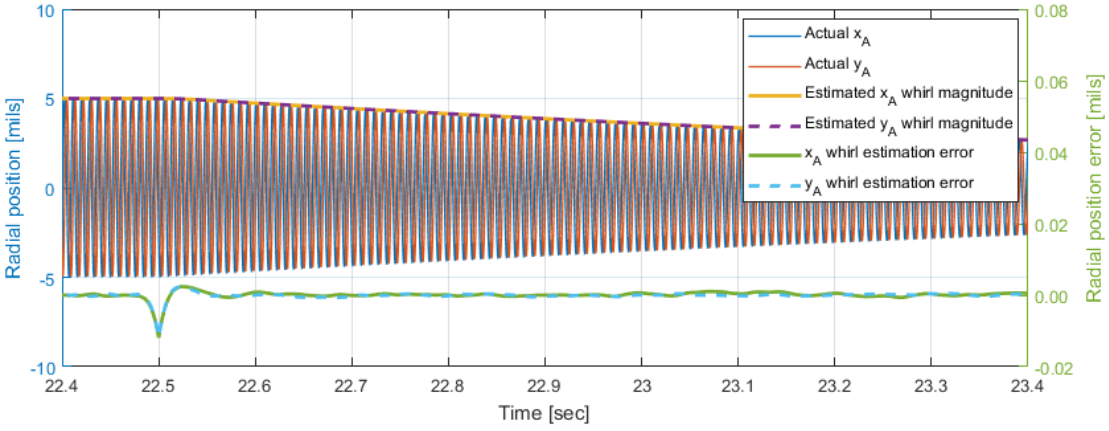

(c)

Figure 3.18: Simulation 2 results for a variable shaft speed of 5,000 to 7,000 RPM: (a) estimated and actual shaft speed and error; (b) estimated and actual 1P radial whirl and error over entire simulation; (c) whirl and error over 22.4 to 23.4 seconds during whirl transient.

Regardless of whether transient conditions influence the shaft speed or the radial whirl, the SWE algorithm correctly estimates these values with negligible errors.

3.2.2. Experimental Results

Experimental data was collected using different offset collets to validate SWE estimation results at various steady state conditions. Test results for Experiment 1, where shaft speed did not exceed 5,000 RPM, is presented in Figure 3.19. The combination of driveshaft runout and offset collet runout is measurable to approximately ± 2 mils (due to machining tolerances of measurement surfaces, analog dial-indicator accuracy, and sufficient clearance to measure dimensions). SWE whirl estimates for toothed wheel *A* match collet offsets within the margin of measurement error; x_A and y_A 1P estimations at 5,000 RPM were within ± 2 mils of the values listed in Table 3.7. The whirl amplitude also increased slightly as speed increased from 3,000 to 5,000 RPM, likely the result of self-excited shaft unbalance.

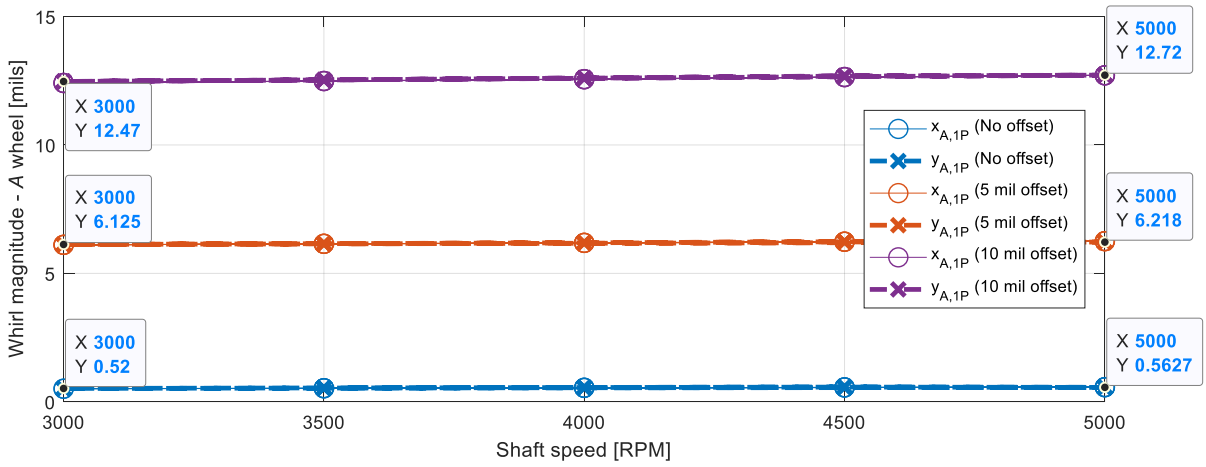

(a)

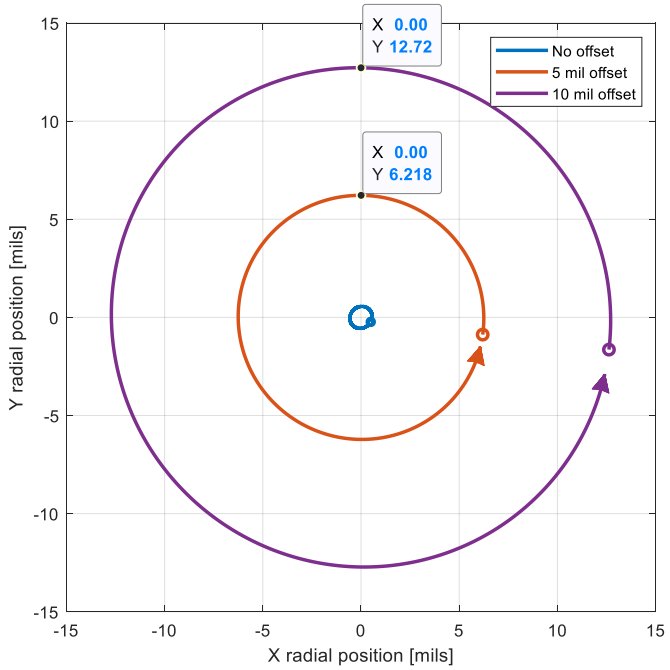

(b)

Figure 3.19: Whirl amplitude estimation during testing with multiple offset collets. a) x_A and y_A 1P whirl amplitudes from 3,000 RPM to 5,000 RPM. b) *A* toothed wheel orbital phase plots at 5,000 RPM with different offsets.

Figure 3.19b shows orbital plots of whirl estimates at 5,000 RPM; as expected the rotor motion is circular, indicating ideal collet machining and symmetric rotor stiffness in

both the *x* and *y* directions. In addition, the small circles indicate the zero-angle position, showing the whirl phase and orbital direction, which remained consistent throughout testing – indicating operation below any significant modes.

To assess shaft whirl estimations during transient conditions in Experiment 2, where the shaft speed changed significantly, test data was collected and is presented in Figure 3.20 demonstrating the transient performance of the SWE algorithm. During the shaft speed transient from 3,000 RPM to 12,000 RPM, the whirl amplitude increased through a resonance at 11,500 RPM resulting in whirl approaching 3 mils on the *B* wheels – exactly what is expected based on the modal survey shown in Figure 3.16. Additionally, the shaft speed increase corresponded to a decrease in the calculated standard deviation as expected due to higher signal voltages at higher shaft speeds. A lower standard deviation indicates a higher effective resolution of the whirl estimate at higher shaft speeds.

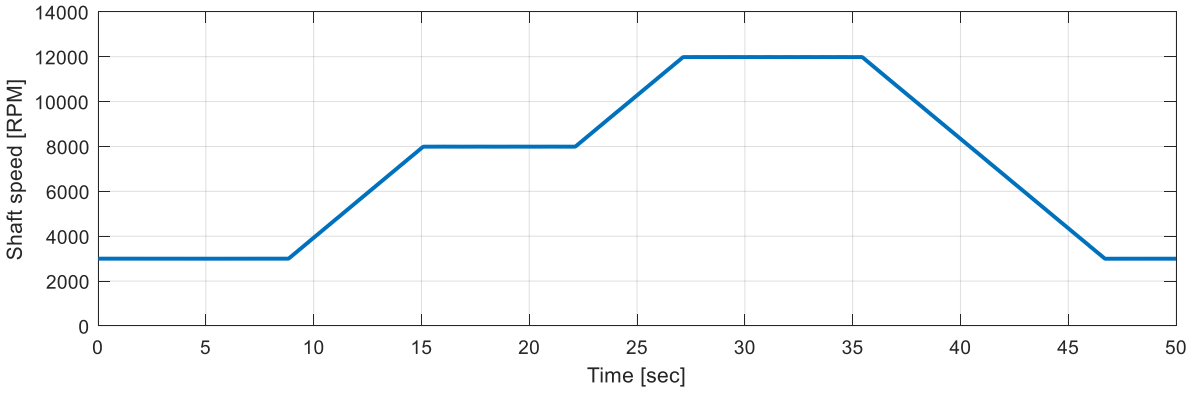

(a)

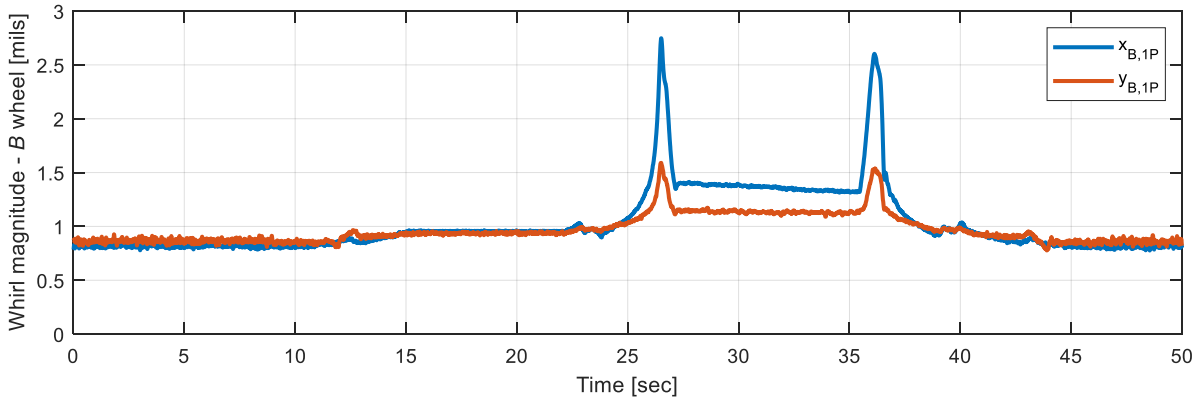

(b)

Figure 3.20: Whirl amplitude estimation during shaft speed transients 3,000 RPM to 12,000 RPM. a) shaft speed profile b) x_B and y_B 1P whirl amplitudes

A shift in whirl amplitude, while the shaft speed was 11,500 RPM occurring at approximately 26.5 and 36.1 seconds, was observed. Whirl orbital plots of the transient profile are shown in Figure 3.21 which indicate that the orbital shape became wider in the *x* direction when transitioning through this resonant frequency; the whirl magnitude decreased following the transition through resonance, however, when above resonance a permanent phase shift occurred. This resonant orbital shape is visible despite its occurrence during a fraction of a second during shaft speed transients, demonstrating the SWE algorithm's ability

to estimate real-time whirl during shaft speed transients – an important diagnostic tool to assess the health of a high-speed drivetrain in avoiding resonance.

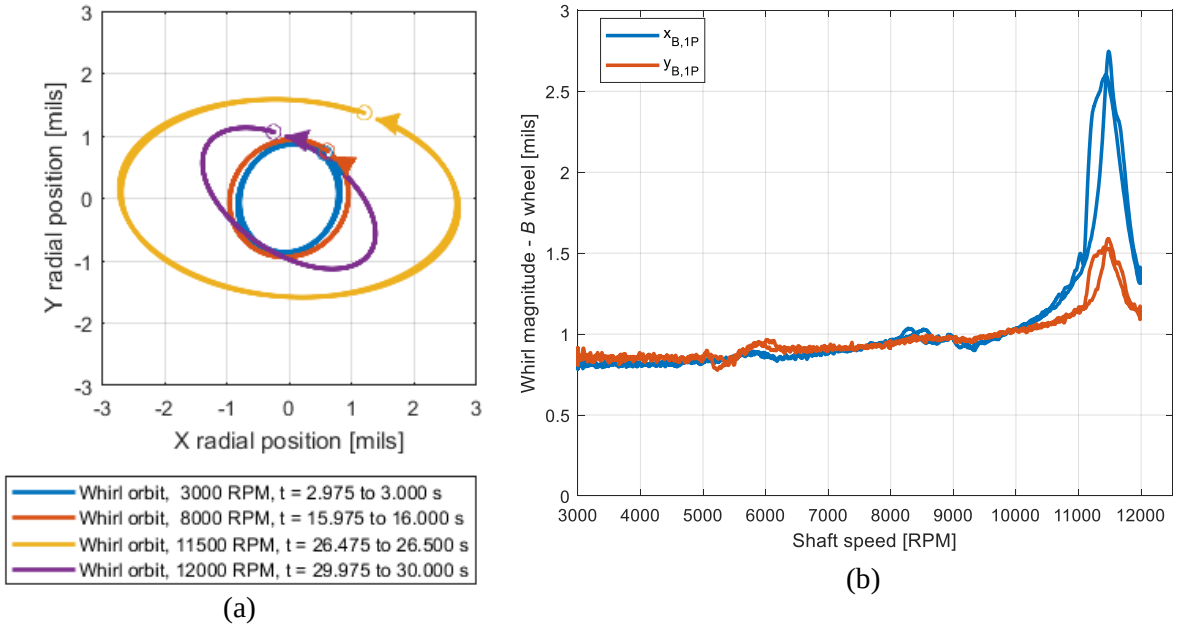

Figure 3.21: a) orbital phase plots (*B* wheel) at various speeds before and after resonance, b) whirl magnitude increase as a function of shaft speed

In Experiment 1, where machined collets produced perfectly circular whirl, the SWE algorithm estimated the collet offset accurately during steady state conditions. Likewise, in Experiment 2, where there was no machined offset, the SWE algorithm demonstrated the capability to measure changes in whirl which follow shaft speed transients. High-speed drivetrains and super-critical engine shafts exhibit conditions similar to both experiments, confirming that this health monitoring functionality can be extended to these applications.

3.3. Discussion

The proposed algorithm and experimental setup solved an industry issue by using rugged VR sensors and timing measurements to calculate the shaft whirl. Simulations and experimental results confirmed that the SWE algorithm, which used data from stationary VR sensors and toothed wheels, accurately estimated speed, static radial translation, and shaft synchronous radial whirl in high-speed rotating shafts. Simulations, which predicted the algorithm's measurement capability, revealed accurate estimation of whirl values to maximum errors less than 0.1 mils – whether shaft speed was constant or variable. Furthermore, simulations suggested that the SWE algorithm could be implemented on an embedded microcontroller performing real-time shaft whirl measurements.

Calibration with static radial translation (to accuracies less than 1 mil) successfully scaled the SWE algorithm estimates of shaft whirl, where experimental results indicated whirl estimates were accurate at the various 0, 5, and 10 mil nominal shaft offsets. Quantifying exact estimation error was difficult because measuring the true shaft orbit independent of the SWE algorithm involved part tolerance stackups and dial-indicator readings resulting in a ± 2 mil validation accuracy. At different offsets, the circular whirl orbit indicated that the stiffness was symmetric, and the majority of radial whirl originated from the collet's machined offset (due to the measurement's circular shape and consistent phase). Discrepancies between the estimated radial whirl and the projected drivetrain runout originated from self-excited shaft unbalances where the offset shifted the toothed wheel CG from the shaft centerline. Due to the high accuracy of static radial translation, the increased whirl estimation resulted from physically increased shaft whirl. At transient whirl conditions

where the speed varied significantly during fractions of a second, the SWE algorithm experimentally measured phase changes and resonance at 11,500 RPM and the overall whirl increase associated with higher shaft speeds. The transient measurement capability and accuracy makes this estimation technique suited for high-bandwidth control system and health monitoring applications.

The SWE algorithm and VR sensor array experimentally showed the unique capability to measure whirl accurately during steady-state and transient conditions. This method has applications on high speed drivetrains and engine tip clearance sensing to provide control feedback and health monitoring information in rugged aircraft environments where previous whirl sensing technologies have failed.

Chapter 4: Concluding Remarks

The overall objective of the VR sensing system research was to develop accurate methods to measure axial translation and radial whirl. In the case of the axial translation measurement, additional benefits occur because additional accuracy in other drivetrain measurements (such as torque) can be realized. This is revolutionary for drivetrain sensing technology, as the majority of current VR drivetrain torque measurement systems make use of torque tubes, which require large amounts of torsional deflection (e.g. ~1 or more degrees of twist) and suffer from difficulties in determining the true stiffness of a large driveshaft over an aerospace temperature range, along with compensating for apparent torsional deflection when the driveshaft deflects radially and axially. With radial and axial measurements and modern digital signal processing, smaller true torsional deflections can be measured (<0.5° of twist). In turn, this allows smaller, lighter drivetrain torque measurement systems that can calculate a more accurate torsional stiffness over operating conditions. The end result is a lighter, more accurate torque measurement that can be provided to critical aircraft systems with capability to measure other drivetrain motions for assessing component health.

The radial whirl measurement algorithm successfully measured motion using sensors which are suitable for a rugged aerospace environment. Other sensing techniques, while they are possible, will not meet the necessary environmental requirements for permanent military and civilian aviation applications. With the complex demodulated measurement of the radial whirl in the x-y plane detailed in the SWE algorithm, additional analysis of the

measurements can be performed to determine forward synchronous whirl, reverse synchronous whirl, asymmetric stiffness measurements, and drivetrain modal measurements. Using these algorithms to accurately perform radial whirl measurements in a production aerospace environment will enable the advancement of health monitoring in engines and drivetrains between gearboxes on aircraft.

4.1. Future Work

Ultimately, future testing will move from small scale laboratory demonstrations at low-torque (<2 ft-lbs) to develop the TAP and SWE algorithms, to larger demonstrations using flight hardware on gearbox test rigs that can apply flight representative vibration environments, power, speed, and torque through a drivetrain. An example test rig is shown below in Figure 4.1 that is part of NASA's high-speed helical gear train test facility [70-71].

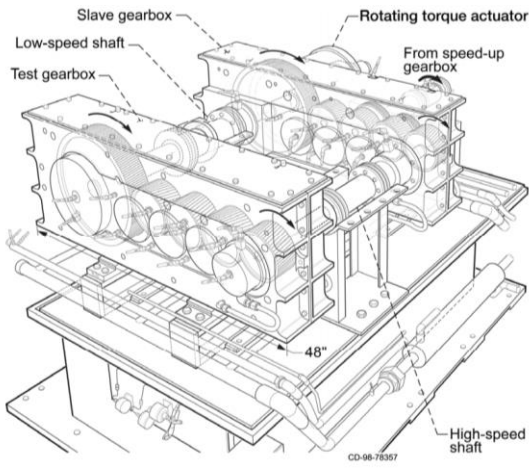

Figure 4.1: NASA high-speed helical gear train test facility capable of testing flight capable VR sensing systems at flight representative power levels

Flightworthy drivetrain components and VR sensor arrays will be tested to assess capability in an aerospace flight environment. Figure 4.2 shows the installation of both

drivetrain components and a VR sensing system around a test stand drivetrain. These drivetrains contain integrated metal teeth allowing VR timing measurements and the application of algorithms defined in this dissertation. Conditions which are testable far exceed testing detailed in this dissertation including shaft speeds up to 13,500 RPM and torques up to 2,000 ft-lbs.

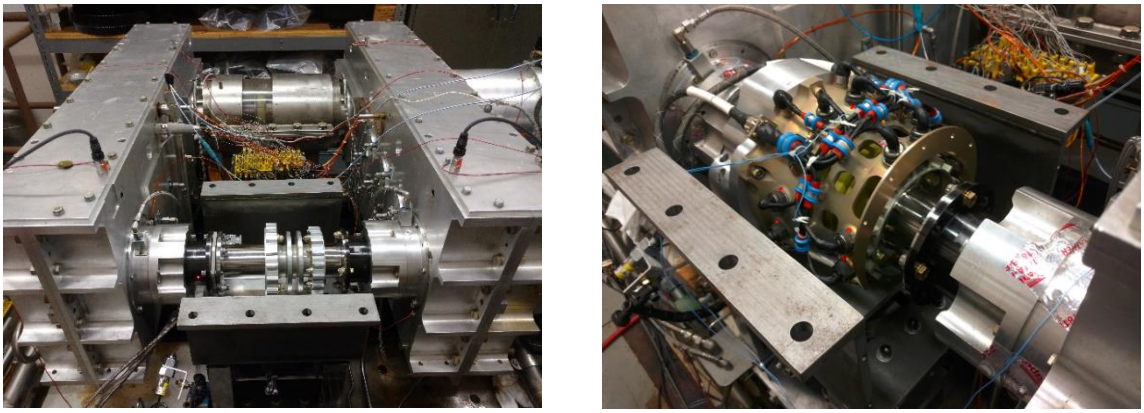

(a) (b)

Figure 4.2: Integration of Flight-worthy drivetrain measurement components on NASA high-speed helical gear train test rig: a) drivetrain installation with integrated teeth on test stand high-speed shaft. b) VR sensor array installed over drivetrain.

Future work on these VR measurement systems will likely include flight testing on aircraft within the next few years to prove the additional axial translation and radial whirl measurements can augment and improve existing VR sensor arrays used for torque measurement.

REFERENCES

[1] Himmelstein S&C., "Avoiding the destructive effects of torsional resonance," in *Technical Memorandum 8150,* 2007.

[2] I. J. Garshelis, C. R. Conto and W. S. Fiegel, "A Single Trasducer for Non-Contact Measurement of the Power, Torque and Speed of a Rotating Shaft," *SAE Technical Paper Series,* Vols. Sensors and Actuators (SP-1066), pp. 57 - 65, 1995.

[3] J. F. Wolfinger, "Electromagnetic Torque Measuring Instrumentation for a Rotating Shaft". United States of America Patent US 4,444,064, 24 April 1984.

[4] S. Mirhakimi, W. E. Earleson and E. W. Ohlson, "Phase Detection Apparatus and Method". United States of America Patent US 5,347,857, 20 September 1994.

[5] G. W. Krutz and M. Evans, "Speed and Torque Sensor for Hydraulic Motor". United States of America Patent 4,593,555, 10 June 1986.

[6] J. G. Irwin III, B. R. Brown, A. M. Rich, M. Schwerke and E. Kocher, "AVMS H-47 Chinook with APAS Tactile Cueing Demonstration Results," in *American Helicopter Society,* West Palm Beach, 2016.

[7] E. Leshner and M. D. Leshner, "Power Inidicating means and method for an Internal Combustion Engine". United States of America Patent 4,064,748, 27 December 1977.

[8] C. Norris and S. Clemens, "Torque Monitoring Apparatus". United States of America Patent 7,810,402, 12 October 2010.

[9] Q. Wang and X. Huang, "Laser Optical Torquemeter". United States of America Patent 5,705,810, 6 January 1998.

[10] R. J. Hazelden, "Optical Torque Sensor". United States of America Patent 5,531,127, 2 July 1996.

[11] W. H. T. Holden, "Torsion Meter". United States of America Patent 2,586,540, 19 February 1952.

[12] R. A. Spinella, "Digital Torquemeter and the Like". United States of America Patent US3888116, 10 June 1975.

[13] J. M. Delvaux and P. P.-L. Sue, "High Resolution Torque Measurement on a Rotating Shaft". USA Patent US 2004/0049357 A1, 11 March 2004.

[14] G. Barg, "Apparatus for the Electronic Measurement of Mechanical Power". United States of America Patent 3,251,223, 17 May 1966.

[15] LORD Microstrain, "WIRELESS TORQUE MONITORING WITH TORQUE-LINK," LORD Corporation, 27 July 2015. [Online]. Available: http://www.microstrain.com/content/wireless-torque-monitoring-torque-link. [Accessed 16 April 2017].

[16] D. O'Neil, C. Townsend and C. Hodgkins, "WIRELESS TORQUE MONITORING FOR UNMANNED ROTORCRAFT FLIGHT TEST APPLICATIONS," LORD Corporation, 19 September 2014. [Online]. Available: http://www.microstrain.com/content/wireless-torque-monitoring-unmanned-rotorcraft-flight-test-applications. [Accessed 16 April 2017].

[17] LORD Microstrain, "Torque Monitoring Solutions," 2014. [Online]. Available: http://www.microstrain.com/sites/default/files/applications/files/appnote-torque.pdf. [Accessed 16 April 2017].

[18] J. Gierut and R. Lohr, "Automotive Powertrain & Chassis Torque Sensor Technology," Honeywell International Inc., 2005.

[19] DEPARTMENT OF DEFENSE INTERFACE STANDARD, "REQUIREMENTS FOR THE CONTROL OF ELECTROMAGNETIC INTERFERENCE CHARACTERISTICS OF SUBSYTEMS AND EQUIPMENT," United States of America Department of Defense, 2015.

[20] I. J. Garshelis, K. Whitney and L. May, "Development of a Non-Contact Torque Transducer for Electric Power Steering Systems," *SAE Technical Paper Series*, Vols. Sensors and Actuators (SP-903), pp. 173-182, 1992.

[21] I. J. Garshelis, J. A. Aleksonis, C. A. Jones and R. M. Rotay, "Development of a Magnetoelastic Torque Transducer for Automotive Transmission Applications," *SAE Technical Paper Series*, Vols. Sensors and Actuators (SP-1220), pp. 35-44, 1997.

[22] Honeywell International Inc., "Advanced Enginer performance for the most demainding environments," 2005. [Online]. Available: https://aerocontent.honeywell.com/aero/common/documents/myaerospacecatalog-

documents/Helicopters-documents/T55-L-714A__CH47_Engine_.pdf. [Accessed 22 April 2017].

[23] R. T. Ehinger and D. R. Bockmiller, "Method and System for Measuring Torque in a Tiltrotor Aircraft". United States of America Patent 2016/0122039A1, 5 May 2016.

[24] D. K. Faymon, T. G. Mulera, P. M. Stevens and M. Shah, "Speed Sensing System with Automatic Sensitivity Adjustment". United States of America Patent US 6,798,192B2, 28 September 2004.

[25] R. M. G. Bodin, "Speed or Torque Probe for Gas Turbine Engines". United States of America Patent US 8,549,931B2, 8 October 2013.

[26] D. A. Dickmeyer, K. G. Maurer and L. L. Redmon, "High Output and Environmentally Impervious Variable Reluctance Sensor". European Patent Application Patent 0571129A1, 05 12 1993.

[27] G. Leucke, Analog and Digital Circuits for Electronic Control System Applications, Burlington, MA: Elsevier, 2005.

[28] M. W. Wilson, "Digital Vernier Torquemeter". United States of America Patent 3,194,065, 13 July 1965.

[29] S. Van Manen, "Torque Monitoring System". United States of America Patent 3,258,961, 5 July 1966.

[30] R. D. Van Millingen and R. T. Portus, "Phasemeters". United States of America Patent US4020685, 27 May 1975.

[31] J. R. Turk, "Horsepower Meter". United States of America Patent 3,640,131, 8 February 1972.

[32] J. R. Witts, "Shaft Torque Measurement". United States of America Patent US 5,067,355, 26 November 1991.

[33] D. A. Goldman, S. Tomasiewicz, V. Ioanna, S. Lacker, P. Rice and H. Wang, "Shaft Sensor Assembly for Angular Velocity, Torque, and Power". United States of America Patent US 6,439,067B1, 27 August 2002.

[34] M. R. Jolly, R. E. Altieri, C. J. Allred, M. Hamel and S. C. Southward, "Torquemeter with improved accuracy and method of use". United States of America Patent US2016/0123821A1, 5 May 2016.

[35] J. R. Parkinson, "Two Sensor Torque Measuring Apparatus with Compensation for Shaft Misalignment". United States of America Patent US3824848, 23 July 1974.

[36] S. C. Southward, "Method and System for Measuring Torque". United States of America Patent US7093504B2, 22 August 2006.

[37] D. E. Kakaley, R. E. Altieri, M. R. Jolly and V. Zaccardo, "Methods and Systems for Measuring Parameters of Rotating Shafts and Couplings". United States of America Patent US Provisional 62/486170, 17 April 2017.

[38] S. Dunkerley, "On the Whirling and Vibration of Shafts," *Proceedings of the Royal Society of London,* vol. 54, pp. 365-370, 1893.

[39] W. J. M. Rankine, "Centrifugal Whirling of Shafts," in *A Manual of Machinery and Millwork*, London, Charles Griffen and Company, 1883, pp. 549-552.

[40] E. Swanson, C. D. Powell and S. Weissman, "A Practical Review of Rotating Machinery Critical Speeds and Modes," May 2005. [Online]. Available: http://sandv.com/downloads/0505swan.pdf. [Accessed Dec 2018].

[41] W. J. Olsson and R. L. Martin, "B747/JT9D Flight Loads and Their Effect on Engine Running Clearances and Perfomance Deterioration: Nacelle Aerodynamic and Inertial Loads (NAIL)/JT9D Jet Engine Diagnostics Programs," NASA CR-165573, 1982.

[42] R. Ruiz, B. Albers, W. Sak, K. Seitzer and B. M. Steinetz, "Benefits of Improved HP Turbine Active Clearance Control," in *NASA Seal/Secondary Air System Workshop, NASA/CP—2007-214995/VOL1*, 2006.

[43] B. L. Newkirk and H. D. Taylor, "Shaft Whipping Due to Oil Action in Journal Bearings," *General Electric Review,* vol. 28, pp. 559-568, 1925.

[44] B. L. Newkirk, "Shaft Whipping," *General Electric Review,* vol. 27, p. 169, 1924.

[45] M. L. Adams and J. Padovan, "Insights into Linearized Rotor Dynamics," *Journal of Sound and Vibration,* vol. 76, no. 1, pp. 129-142, 1981.

[46] E. J. Gunter, "The Influence of Internal Friction on the Stability of High Speed Rotors," *Journal of Engineering for Industry*, pp. 683-688, 1967.

[47] E. Pollman, H. Schwerdtfeger and H. Termuehlen, "Flow Excited Vibrations in High-Pressure Turbines (Steam Whirl)," *Journal of Engineering for Power,* vol. 100, no. April, pp. 219-228, 1978.

[48] J. S. Alford, "Protecting Turbomachinery from Self-Excited Rotor Whirl," *Journal of Engineering for Power ASME,* vol. A, no. 4, pp. 333-343, 1965.

[49] M. L. Adams, Jr., Rotating Machinery Vibration: From Analysis to Troubleshooting, Boca Raton, FL: CRC, 2010.

[50] S. B. Lattime and B. M. Steinetz, "Turbine Engine Clearance Control Systems: Current Practices and Future Directions," NASA/TM-2002-211794, 2002.

[51] H. H. Jeffcott, "The Lateral Vibration of Loaded Shafts in the Neighbourhood of a Whirling Speed -- The Effect of Want of Balance," *Philosophical Magazine Series 6,* vol. 37, no. 219, pp. 304-314, 1919.

[52] J. Binghui and Z. Xiaodong, "An optical fiber Blade Tip Clearance Sensor for Active Clearance Control Applications," *Procedia Engineering,* vol. 2011, no. 15, pp. 984-988, 2011.

[53] G. Schweitzer and E. H. Maslen, "An Example of Unbalance Control," in *Magnetic Bearings: Theory, Design, and Application to Rotating Machinery*, Berlin Heidelberg, Springer-Verlag , 2009, pp. 220-224.

[54] E. Hoffman, "TURBINE BLADE FAILURE ROCKS PASSENGER PLANE WITH 359 ON BOARD," 11 July 2017. [Online]. Available: https://www.lsptechnologies.com/turbine-blade-failure-passenger-plane/. [Accessed Dec 2018].

[55] S. Hradecky, "Report: National Jet B712 at Newman on Jul 13th 2007, engine failure," 7 April 2009. [Online]. Available: http://avherald.com/h?article=417ae83c. [Accessed Dec 2018].

[56] B. Rebbechi, M. Burchill and G. Coco, "An Investigation of F/A-18 AMAD Gearbox Driveshaft Vibration," Commonwealth of Austrailia: DSTO Aeronautical and Maritime Research Laboratory Department of Defence, DSTO-TN-0121, 1997.

[57] W. J. M. Rankine, "On the Centrifugal Force of Rotating Shafts," *The Engineer,* vol. XXVII, no. January to June, p. 249, 1869.

[58] E. J. Gunter, "Dynamic Stability of Rotor Bearing Systems," NASA: Scientific and Technical Information Division, NASA SP-113, 1966.

[59] F. C. Nelson, "A Brief History of Early Rotor Dynamics," *Sound and Vibration,* vol. 37, no. 6, pp. 8-11, 2003.

[60] W. Kerr, "On the Whirling Speeds of Loaded Shafts," *Engineering,* p. 150, 1916.

[61] J. R. Parkinson, "Apparatus for Detecting Torque, Axial Position, and Axial Alignment of a Rotating Shaft". United States of America Patent US6782766B2, 31 August 2004.

[62] J. R. Parkinson, "Monitoring Apparatus for Detecting Axial Position and Axial Alignment of a Rotating Shaft". United States of America Patent US 5,508,609, 16 April 1996.

[63] J. R. Parkinson, "Thrust-Meter Utilizing a Phase Measurement System for Thrust Measurement". United States of America Patent US3851525, 3 December 1974.

[64] F. P. Beer, E. R. Johnston, Jr., J. T. Dewolf and D. F. Mazurek, Mechanics of Materials, Sixth Edition, New York, NY: McGraw-Hill, 2012.

[65] D. E. Kakaley, R. E. Altieri and G. D. Buckner, "Non-Contacting Measurement of Torque and Axial Translation in High-Speed Rotating Shafts," *Submitted to Mechanical Systems and Signal Processing,* 2017.

[66] D. Culley, "Recent Technology Advances in Distributed Engine Control," in *Aerospace Control and Guidance Systems Committee (ACGSC),* Fairborn, OH, 2017.

[67] M. S. Alencar and V. C. d. Rocha, "Quadrature Amplitude Demodulation," in *Communication Systems*, New York, NY, Springer Science & Business Media, 2005, p. 182.

[68] CRC, CRC Handbook of Chemitry and Physics, New York: McGraw, 1970.

[69] R. C. Soderberg, "On the Subcritical Speeds of the Rotating Shaft," *American Society of Mechanical Engineers*, vol. 54, no. 4, pp. 45-52, 1932.

[70] R. Handschuh, C. Kilmain and R. Ehinger, "Operational Condition and Superfinishing Effect on High-Speed Helical Gearing System Performance," NASA TM-2007-214696, 2007.

[71] R. F. Handschuh, R. Ehinger, E. Sinusas and C. Kilmain, "Double Helical Gear Performance Results in High Speed Gear Trains," NASA TM-2010-216760, 2010.